Oxide-Confined VCSELs for High-Speed Optical Interconnects

Milton Feng, *Life Fellow, IEEE*, Chao-Hsin Wu, *Member, IEEE*, and Nick Holonyak, Jr., *Life Fellow, IEEE*

(Invited Paper)

***Abstract*— The electrically pumped vertical-cavity surface-emitting laser (VCSEL) was first demonstrated with metal cavities by Iga (1979); however, the device threshold current was too high. Distributed Bragg reflector cavities proposed by Scifres and Burnham (1975) were adopted to improve the optical cavity loss. Yet, it was not a practical use until the discovery of the native oxide of AlGaAs and the insertion of quantum wells to provide simultaneous current and optical confinement in semiconductor laser by Holonyak and Dallesasse (1990). Later, the first "low-threshold" oxide-confined VCSEL was realized by Deppe (1994) and opened the door of commercial application for a gigabit energy-efficient optical links. At present, we demonstrated that the oxide-confined VCSELs have advanced error-free data transmission [bit-error rate (BER) $\leq 10^{-12}$]to 57 Gb/s at 25 °C and 50 Gb/s at 85 °C, and also demonstrated that the pre-leveled 16-quadrature amplitude modulation orthogonal frequency-division multiplexing data were achieved at 104 Gbit/s under back-to-back transmission with the received error vector magnitude, SNR, and BER of 17.3%, 15.2 dB, and 3.8×10^{-3}, respectively.**

***Index Terms*— Optical interconnect, oxidation, semiconductor laser, vertical-cavity surface-emitting lasers (VCSELs).**

I. Introduction

THE oxide-confined vertical-cavity surface-emitting laser (Oxide-Confined VCSEL) is considered to be an important semiconductor device for short-range optical interconnect and high-performance computer due to the growing demand of faster access to large amounts of information. Nowadays, traditional copper-based interconnects have been gradually replaced by short-haul optical links based on 850 nm wavelength optical transceivers and multimode fibers to solve the issues of power consumption, signal distortion, electromagnetic interference, cross talk, and most importantly the bandwidth requirement. The VCSEL, the unique semiconductor light sources apart from the edge-emitting lasers, provides an efficient data processing and transmission way inside data centers owing to its low threshold current and power consumption, high modulation speed, small footprint, a near-circular optical beam for coupling, high reliability, easy packaging and forming dense arrays, and inexpensive on-wafer testing. Today, the Oxide-Confined VCSELs employed quantum wells (QWs) in the active region and oxide-confined apertures have revolutionized our daily life from data centers to 3D sensing applications. QWs can effectively enhance the radiative recombination processes and oxide-confined apertures to further make VCSELs into practical use with small active volumes and lower threshold currents. These two features are closely related to the laser modulation bandwidth and transmission data rate.

Due to the high-Q microcavity formed by DBRs and an oxide-confined aperture, a Purcell enhancement of electron-hole spontaneous lifetime can be achieved and readily determined by microwave measurements [1], [2]. The optical mode volume of the microcavity can determine the laser mode spacing and mode number, resulting in the effect on low threshold, fast recombination lifetime, and high-speed modulation of VCSELs [3]. The radiative recombination lifetime can be extracted and analyzed using microwave method to provide further insight into the design of layout and material toward large laser bandwidth and better signal integrity [4]. The energy efficient transmission of 20 and 40 Gb/s eye diagrams using VCSELs with a bandwidth of 18.7 GHz was then demonstrated with an oxide-confined microcavity design [5]. An enhanced bandwidth of 22.6 GHz with low relative intensity noise (RIN) approaching to standard quantum limit was reported in the microcavity VCSELs. The smaller optical dimension determined by oxide aperture exhibits lower RIN due to reduced carrier fluctuation and mode competition inside the laser cavity [6]. Later in 2014, a 40 Gb/s error free transmission with 431 fJ/Bit was presented in the 4 μm oxide aperture VCSELs [7]. The importance of careful control of oxidation process and optical mode was emphasized in both

Manuscript received January 19, 2018; accepted March 1, 2018. Date of publication March 19, 2018; date of current version March 30, 2018. This work was supported in part by Dr. M. Gerhold of the Army Research Office under Grant W911NF-17-1-0112, in part by Dr. K. C. Goretta of Air Force of Scientific Research under Grant FA9550-15-1-0122, in part by the Foxconn Interconnect Technology, a leading interconnect company led by UIUC's distinguished alumni, in part by the National Science Foundation under Grant 1640196, and in part by the Nanoelectronics Research Corporation, a wholly-owned subsidiary of the Semiconductor Research Corporation (SRC), through Electronic-Photonic Integration Using the Transistor Laser for Energy-Efficient Computing, an SRC-Nanoelectronics Research Initiative under Grant 2697.001.The work of C. H. Wu was supported by the Ministry of Science and Technology of Taiwan under Grant 106-2218-E-005-001, Grant 106-2622-E-002-023-CC2, Grant 105-2628-E-002-007-MY3, and Grant 106-2923-E-002-006-MY3. *(Corresponding author: Milton Feng.)*

M. Feng and N. Holonyak, Jr., are with the Department of Electrical and Computer Engineering, Microelectronics and Nanotechnology Laboratory, University of Illinois at Urbana–Champaign, Champaign, IL 61801 USA (e-mail: mfeng@illinois.edu).

C.-H. Wu is with the Department of Electrical Engineering, Graduate Institute of Photonics and Optoelectronics, Graduate Institute of Electronics Engineering, National Taiwan University, Taipei 10617, Taiwan (e-mail: chaoshinewu@ntu.edu.tw).

Color versions of one or more of the figures in this paper are available online at http://ieeexplore.ieee.org.

Digital Object Identifier 10.1109/JQE.2018.2817068

850 nm and 780 nm VCSELs [8]. With careful control of oxidation process, 780 nm VCSELs can reach 13.5 Gb/s with 0.97 pJ/Bit energy efficiency [9]. The effect of aperture size on the RIN and data rates was compared with 40 Gb/s under back-to-back and 100 m OM4 fiber transmission up to 65 °C operation in 2015 [10]. Several reports have also reported over 40 Gb/s error-free data transmission [11]–[15].

To further achieve 50 Gb/s operation, 0.5-λ cavity, 5 quantum-wells and oxidation aperture were employed in the VCSEL design [11], [16], [17]. In 2016, a 5 μm VCSEL with 28.2 GHz bandwidth and 50 Gb/s error-free transmission was achieved by optimization of laser series resistance [17]. Later in 2016 we demonstrated 57 Gb/s error-free operation at room temperature and 50 Gb/s operation up to 85 °C [18], [19]. The microwave extraction methods to determine radiative recombination lifetime and to model small-signal equivalent circuit of VCSELs were performed. The extracted intrinsic modulation bandwidth is 31.86 GHz and 26.19 GHz at room temperature and 85 °C, respectively [20]. The temperature sensitivity can be further alleviated in terms of optical output and threshold current change, resulting in an improvement of budget penalty for 50 Gb/s operation at 85 °C in 2017 [21]. Recently, we have achieved error-free data transmission for a 100 meter multimode fiber (MMF) with a record data rate of 46 Gb/s at 25°C, 43 Gb/s at 75°C and 42 Gb/s at 85°C without the use of signal processing such as equalizer or forward error correction [22]. The record performance of 850 nm oxide-confined VCSELs shows the importance of optimizing lower threshold current and microcavity mode to minimize the modal dispersion in OM4 fiber.

In this report, we begin with a review of the VCSEL's history and the discovery of III-V oxidation for current and optical confinement in semiconductor lasers. These have then led to the realization of ultralow threshold oxide-confined VCSELs that have set the foundation of today's energy-efficient optical interconnect. The pathway to high-speed VCSELs and their characteristics are summarized from the effect of microcavity design to small-signal modeling and parameters extraction. Oxide-confined VCSEL operated up to 85 °C, achieved record performance of 50 Gb/s error-free data transmission without the use of equalizers under 3 meter multimode fiber (OM4 -MMF) and 42 Gb/s data transmission up to 100 meter OM4 MMF. Lastly, transmission using orthogonal frequency- division multiplexing (OFDM) will be presented to show the possibility toward larger transmission capacity of the oxide-confined VCSELs.

II. Innovation of Oxide-Confined VCSELs

A. History of VCSELs

The first demonstration of a semiconductor diode laser was in 1962 by Hall *et al.* [23] with an infrared (IR) wavelength and by Holonyak and Bevacqua [24] with a visible (Red) wavelength. The lasers were operated with optical cavities in which the coherent light propagated parallel to the crystal surface, which are known as "edge-emitting" lasers today. With addition of a heterojunction for carrier and field confinement in 1970, the diode laser was able to operate at room temperature [25], [26]. Quantum wells (QWs) were then added in the active regions of semiconductor diode laser to further improve the optical output in 1977 [27], [28]. This is a significant accomplishment, considering all the LEDs and semiconductor laser are made of quantum-wells and MOCVD technology today.

On the other hand, the demonstrations of "surface-emitting" lasers with different pumping mechanisms were reported in 1964 to 1966 [29]–[31]. The first current-injected surface-emitting lasing operation was achieved by Melngailis with a 5.2 um wavelength in a 220 μm long cavity made from n^+np^+ doped InSb with a polished surface and Ag-Au contact. Even though it was under pulsed operation at temperature of 10 K, several advantages we are familiar with today were already mentioned to such a structure, such as small beam divergence, array formation, and large output powers. The first p-n junction-based electrically-pumped SEL was demonstrated by the Iga group from the Tokyo Institute of Technology in 1979 [32]. This work incorporated a 1.8 um InGaAsP active region with metal as the reflective mirror to form a resonant cavity. They demonstrated a threshold current density of 44 kA/cm^2 under pulse current injection at 77 K.

To reduce the SEL threshold current, the reduction of active cavity volume and metal cavity loss are required. This means the necessary reflectivity for each mirror of cavity must be very high ($\sim$ 99.9 %). Another improvement is to shift the material system to wider bandgap, such as AlGaAs/GaAs, to reduce the Auger recombination sufficiently to enable pulsed injection room temperature operation, which was demonstrated in 1984 [33], [34]. For metal reflectors, such as thick Au films, the reflectivity is limited to 98 % due to the high optical absorption; thus they are not for practical uses. Dielectric materials, such as semiconductors at photon energies below their bandgap, are more desirable due to a very low absorption coefficient. In a multilayer structure (Bragg reflector) the reflection from many interfaces may add in phase to produce a large reflection over 99.99 % at a loss less than 1 cm^{-1}. With the combination of deposited dielectric and/or metal mirrors, the continuous-wave and room-temperature operation of SEL was achieved in 1989 [35]–[37]. While dielectric mirrors (e.g. TiO_2/SiO_2) have shown improvement on laser performance [35], the research works focusing on semiconductor reflectors using alternating semiconductor layers have suggested another approach toward practical VCSELs [38], [39]. In 1987, Ogura *et al.* [40] reported a novel distributed feedback surface-emitting laser firstly using AlGaAs/GaAs mirrors. The active volume in this work was still large and the carrier injection was not very efficient. Iga's group in 1988 has used epitaxially grown AlGaAs/AlAs Bragg reflector by metal-organic chemical vapor deposition (MOCVD) to form SEL [41]. In 1989, Lee and Jewell demonstrated the significant improvement using full top and bottom semiconductor DBR with very high reflectivity mirror (R $\sim$ 99.9%), resulting in a small active volume [42], [43]. The threshold current density was able to reduce to 1.8 kA/cm^2. In addition, they employed compressively strained $In_{0.2}Ga_{0.8}As$/GaAs quantum wells to enhance optical gain in the TE polarization due to the splitting of the heavy and light hole states. The emission wavelength

from InGaAs quantum wells is around 980 nm, which is transparent to GaAs substrate, and makes possible of multilayer of AlAs/GaAs structure with little absorptive loss. To this point, the VCSEL became a useful device operated at low powers and room temperature.

B. The Discovery of III-V Oxide & Oxide-Confined VCSELs

The oxidation process to form apertures for electrical and optical confinement as well as the reduction of sidewall leakage current (surface states) is a standard production step in manufacturing low threshold VCSELs. The discovery of III-V oxidation process was first reported at the University of Illinois at Urbana-Champaign by Dallesasse *et al.* [44] in 1989. An elevated temperature water vapor process was developed for the oxidation of high composition Al_x $Ga_{1-x}As$ to form high quality transparent native oxides. A strong crystallographic preference was found as well. The III-V oxidation process was then applied in edge-emitting QW lasers [45]. The oxide was used for current confinement and resulted in a sharp turn-on and single mode operation. Multistripe laser arrays were then demonstrated with different oxidation depths to control the coupling between adjacent stripes [46]. The results identified that the oxide could be used for both electrical and optical confinement. The use of lateral oxidation to form edge-emitting lasers [47], and the work on III-V oxide field-effect transistors were also demonstrated [48]. Wide bandwidth high reflectivity DBR mirrors was formed by selective oxidation of AlAs as the low refractive index layer and GaAs as the high refractive index layer [49], [50].

Before the III-V oxidation process was invented, the proton implant process had used to provide current confinement in VCSELs [51], [52]. Proton implanted VCSELs have been commercialized for Gigabit Ethernet by many companies in the past. Although the proton implant could provide good electrical confinement, it couldn't improve the optical confinement in the transverse direction. In 1994, the first demonstration of an oxidation process for controlling the "oxide-defined apertures" to form a small volume of optical cavity and providing current confinement in VCSELs was achieved with sub-mA threshold by the Deppe group [53]. With the selective oxidation process, the VCSEL operated continuously at room temperature and low threshold of 225 μA was achieved. A detailed report of the III-V oxidation process applied to VCSELs can be found in [54]. Following Deppe's publications, other groups began to incorporate "oxide confined apertures" into VCSELs and integrated full top and bottom DBRs [42], [43] and reported later in 1994 [55].

III. High Speed Data Rate Oxide-Confined VCSELs

A. Microcavity Optical Mode and Purcell Effect

The modulation bandwidth and data transmission capability of the oxide-confined VCSELs are thermally limited by the junction temperature due to the high current density in a small volume and rely on several factors, such as quantum well design, resonance cavity, e-h recombination lifetime, photon lifetime, impedance match, parasitic resistance and capacitance, thermal impedance, heat removal, etc.

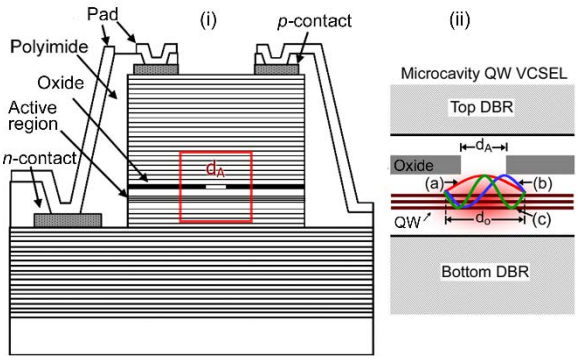

Fig. 1. (i) Schematic cross-section of microcavity VCSEL device. (ii) The microcavity shows the allowed optical modes: (a) 1st order mode, (b) 2nd order mode, and (c) 3rd mode.

Previous studies more focused on the device structure and material design of pn junction based of oxide-confined VCSELs [12]–[15], [56]–[62]. To further improved the thermally limited bandwidth, recently, Deppe's group has proposed and demonstrated new VCSELs without the use of oxidation confined apertures and use of lithographic defined aperture to achieve record low differential resistance and reduction of junction temperature [63]–[65]

Furthermore, the novel idea was to change the device platform from diode to transistor structure to improve spontaneous recombination lifetime. A "tilted-charge" population in the active region of QW-embedded heterojunction bipolar light-emitting transistors (HBLETs) can be established through a third terminal, the collector, to remove slow-recombining carriers and significantly improve the recombination lifetime from nanosecond in pn-junction diode to pico-second range. Due to fast recombination lifetime, the resonance-free optical response of transistor lasers (TLs) incorporated with oxidation process was demonstrated [66]–[71].

In the case of diode lasers, a saturated carrier profile in the active region limits the average recombination lifetime only a nano-second. Purcell proposed in 1946 that the transition rate of upper-state and lower-state (referred to electron-hole spontaneous recombination rate by most of researchers in semiconductor devices) could be enhanced in a small volume microcavity with a high Q [72]. This brings out the idea of low threshold light-emitting devices. The VCSEL structure turns out to be the perfect device to provide a high Q cavity rather than nano-pillar structures. The lateral oxidation in VCSEL can be tailored to confined a small optical cavity. Therefore, we began from focusing on the spectral and microwave behavior of the VCSEL form of microcavity laser to pursue high-speed operation. The device with smaller volume exhibits lower threshold current, lower relative intensity noise (RIN), larger mode spacing, larger side-mode suppression ratio (SMSR), and higher modulation bandwidth and data transmission rate.

The schematic cross section of the microcavity VCSEL is shown in Fig. 1(i). Figure 1(ii) indicates the possible optical modes introduced inside the microcavity: (a) 1st order (fundamental), (b) 2nd order, and (c) 3rd order mode. The oxide

aperture diameter is d_A, and d_0 is the lateral optical mode dimension. Here three devices with different aperture sizes are processed: D1 (2 μm), D2 (2.5 μm), and D3 (3.5 μm). The oxide-confined aperture improves the overlap of electrical and optical gain owing to better confinement of the optical field and the current injection, further defining the lateral optical mode dimension. Together with the vertical DBR mirror, a microcavity laser is readily formed without suffering high input impedance and optical scattering loss using a pillar structure. The merit of the microcavity is in providing a low laser threshold due to "easier" single-mode operation, and finally threshold-less operation.

A smaller cavity allows the electromagnetic wave to exist only in a few modes, say, the fundamental mode and a couple of higher order modes as shown in Fig. 1(ii). For an oxide-confined microcavity VCSEL of aperture size $d_A > 5$ μm the optical mode is approximately circular, but for smaller aperture size $d_A < 5$ μm the optical mode profile will be elliptical-like owing to the sensitivity of the oxidation procedure and crystal anisotropy. Ideally, from spectral data on different modes we can extract the lateral modal profile by solving the Helmholtz equation numerically under given boundary condition.

For a rough estimate we assume the optical field is confined laterally inside the mode boundary, and approximate the optical mode profile as rectangular with width a and length b. Since the carrier distribution and optical lateral dimension profile will change at different bias current levels, it is necessary to calculate a, b, and L for each bias current. By solving the Helmholtz equation

$$\left(\frac{\partial^2}{\partial x^2}+\frac{\partial^2}{\partial y^2}\right)E(x,y)+(k_0^2\tilde{n}^2-k_z^2)E(x,y)=0 \qquad (1)$$

we obtain the Eigen-mode solution satisfying the expression for both the transverse electrical and transverse magnetic field,

$$k_0^2(m,n)=\frac{\omega^2}{c^2}=\frac{1}{\tilde{n}^2(r)}\left[k_z^2+\left(\frac{m\pi}{a}\right)^2+\left(\frac{n\pi}{b}\right)^2\right] \quad (m,n=1,2,3,.....) \qquad (2)$$

$$k_z=\frac{l\pi}{L}, \quad (l=1,2,\ldots) \qquad (3)$$

The quantity $k_0(m, n)$ is the propagation constant in vacuum, L is the upper and lower Bragg reflector spacing in the vertical direction, and $\tilde{n}$ is the effective refractive index inside the aperture.

In Fig. 2 three optical emission spectra are shown for three different microcavity VCSELs operating above threshold at a fixed current I = 0.8 mA (I_{TH} = 0.15, 0.16, and 0.20 mA for D1, D2, D3, respectively). From the spectral measurements of Fig. 2 we can clearly identify for each device the wavelength of each optical mode: 1st mode (fundamental) $\lambda(1,1)$, 2nd modes $\lambda(1,2)$ and $\lambda(2,1)$, 3rd modes $\lambda(2,2)$, $\lambda(1,3)$, and $\lambda(3,1)$, and then higher order modes. From these data we can estimate the modal dimensions a and b as well as the upper and bottom DBR spacing L. From spectral data we estimate the mode

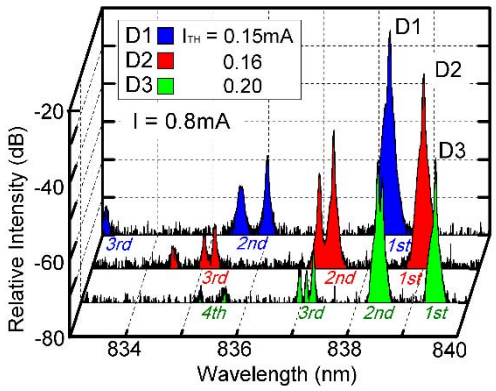

Fig. 2. Relative spectral intensity at fixed bias current $I = 0.8$ mA for three different VCSEL devices D1, D2 and D3. The label "1st" indicates the fundamental mode, "2nd" the second order modes, and "3rd" the third order modes. For D1 the mode spacing is $\Delta\lambda = 2.22$ nm, $I_{th} = 0.15$ mA; for D2 $\Delta\lambda = 1.6$ nm, $I_{th} = 0.16$ mA; and for D3 $\Delta\lambda = 1$ nm, $I_{th} = 0.20$ mA.

TABLE I
MICROCAVITY VCSEL OPTICAL MODE DIMENSION AT BIAS I = 0.8mA

	I_{TH} (mA)	$\Delta\lambda$ (nm) (I = 0.8mA)	a (Width) (μm)	b (Length) (μm)	L (~$\lambda/\tilde{n}$) (μm)
D1	0.15	2.22	2.73	3.02	0.2546
D2	0.16	1.6	3.28	3.53	0.2546
D3	0.20	1.0	4.41	4.59	0.2546

dimensions a, b, and L using Eqs. (4) to (6) as

$$k_0^2(2,1)-k_0^2(1,1)=\left[\frac{2\pi}{\lambda(2,1)}\right]^2-\left[\frac{2\pi}{\lambda(1,1)}\right]^2=\frac{3\pi^2}{\tilde{n}^2a^2}, \qquad (4)$$

$$k_0^2(1,2)-k_0^2(1,1)=\left[\frac{2\pi}{\lambda(1,2)}\right]^2-\left[\frac{2\pi}{\lambda(1,1)}\right]^2=\frac{3\pi^2}{\tilde{n}^2b^2}, \qquad (5)$$

$$L=\frac{2\pi}{k_z}=\frac{2\pi}{\sqrt{\left[\frac{2\pi\tilde{n}}{\lambda(1,1)}\right]^2-\left(\frac{\pi}{a}\right)^2-\left(\frac{\pi}{b}\right)^2}}. \qquad (6)$$

In Table I we summarize the calculated mode dimensions a, b, and L for three different aperture sizes at bias current I = 0.8 mA. The data show the cavity vertical distance L is more than 10 times smaller than the lateral dimension a and b; hence, the fundamental mode wavelength is mainly determined by L as $\lambda(1,1) \approx \tilde{n}L$. The mode dimensions a and b determine the mode spacing $\Delta\lambda$ between the fundamental mode and the 2nd order modes. As shown in Table I, oxide-aperture size reduction decreases the lateral mode dimensions and enlarges the mode spacing $\Delta\lambda$. This shows that optical mode control can be achieved by "tuning" the oxide aperture size as well as by the vertical cavity length.

To achieve lower threshold current VCSELs, we design the position of the maximum gain profile aligned with the fundamental cavity modes. For devices with larger mode spacing, $\Delta\lambda$, there are fewer modes within the gain profile; i.e., the fundamental mode will contribute mainly to the increase in optical intensity (photon density). Carrier re-adjustment in the mode acts as a positive feedback mechanism "tuning" stimulated emission and providing more photon generation in the fundamental mode. With larger mode spacing, the carrier

TABLE II
MICROCAVITY VCSEL PURCELL ENHANCEMENT FACTOR FP AT BIAS I = 0.1mA

	I_{TH} (mA)	$V_{eff} = abL$ (μm^3) (@ I = 0.1mA)	$Q = \lambda/\Delta\lambda_{cav}$ (@ I =0.1mA)	F_P (Purcell Factor)
D1	0.15	2.0	12800	8.0
D2	0.16	3.0	10300	4.3
D3	0.20	5.3	6200	1.5

injection is more "efficiently" concentrated in only one mode. This behavior can be observed from the spectral data in Fig. 2.

Purcell in 1946 predicted that the transition rate between the upper state and lower state in a small volume cavity will be enhanced in the case of a high cavity Q. We can compare a large area VCSEL with an assumed, large, bulk spontaneous lifetime, τ_{Bulk}, to the case of a microcavity laser with reduced electron-hole spontaneous recombination lifetime, τ_{cavity}, by a factor F_P,

$$F_P = \frac{\tau_{Bulk}}{\tau_{cavity}} = \frac{3Q}{4\pi^2 V_{eff}} \left(\frac{\lambda}{\tilde{n}}\right)^3. \quad (7)$$

The Purcell formula indicates that below threshold, F_P can be estimated from the effective mode volume V_{eff}, mode wavelength λ, cavity material index $\tilde{n}$, and cavity $Q = \lambda/\Delta\lambda_{cav}$. Previous work on the Purcell enhancement factor F_P was extracted from time-resolved photoluminescence or phase resolved spectroscopy experiments [73]–[76]. Both methods require optical input-output data, not necessarily making it easy to achieve signal-separation. In contrast, the electrical current driven on microcavity laser method and microwave bandwidth measurement on microcavity laser below threshold method provide excellent isolation via an electrical-input and optical-output to analyze the Purcell effect.

In Table II we summarize the F_P data for three different aperture size devices at bias current I = 0.1 mA (< I_{TH}). The data indicate that a smaller oxide aperture device will have a larger Purcell effect and higher cavity Q. With a faster electron-hole spontaneous emission recombination rate (smaller lifetime), the device can demonstrate ultra-low threshold current. The spontaneous emission lifetime can also be extracted from the microwave frequency response below threshold; the extracted Purcell factor obtained by microwave measurements is consistent with that estimated from spectral measurements.

B. Quantum-Limited Relative Intensity Noise (RIN)

The system noise contains the thermal noise of optical link, the photodetector shot noise and the relative intensity noise (RIN) of laser sources. The laser RIN measures the relative amplitude of optical power fluctuation around the average optical power level and is related to the optical interference between the coherent laser mode and the spontaneous light emission as well as the laser mode competition. A laser with low RIN is essential in the pursuit of high fidelity optical transmission [77]–[80]. Here we investigate the RIN and modulation bandwidth of three VCSELs

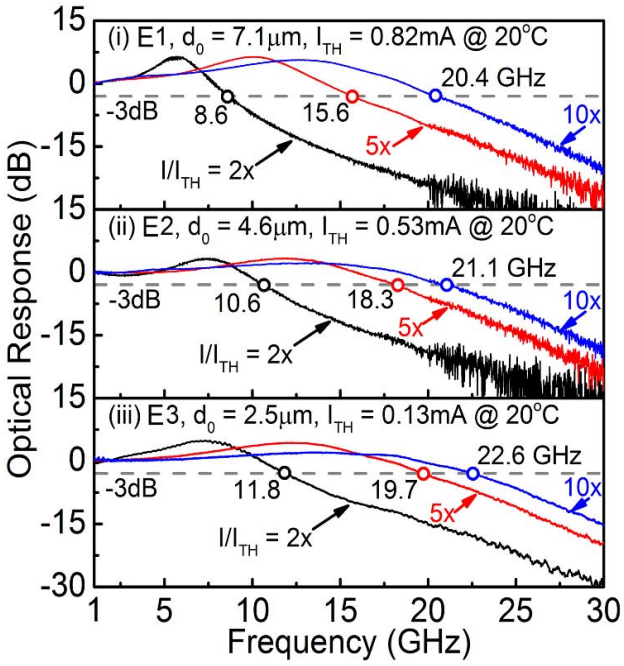

Fig. 3. Measured optical response of VCSEL devices E1, E2 and E3 at I/I_{TH} = 2, 5, and 10. The −3 dB optical modulation bandwidth at I/ITH = 10 is 20.4, 21.1, and 22.6 GHz for E1, E2 and E3, respectively.

(E1, E2, and E3) with different oxide-confined apertures (d_A) and optical modal dimensions (d_0). From the spectrum analysis, we can calculate the lateral optical modal dimensions from the measured mode spacing to be d_0 = 7.1 μm (E1), 4.6 μm (E2), and 2.5 μm (E3). E3 is defined as an oxide-confined microcavity VCSEL due to the reduced oxide aperture dimension (d_A < 3 μm).

Figure 3 displays the measured optical microwave response of VCSEL devices (i) E1, (ii) E2 and (iii) E3 at 20°C for bias setting parameters at I/I_{TH} = 2, 5 and 10. We employ a Parametric Network Analyzer (PNA) with two-port calibration to measure the electrical and optical microwave response of VCSEL devices. When the devices are high biased at I/I_{TH} = 10, the −3 dB bandwidth (f_{-3dB}) increases from 20.4 GHz (E1) to 21.1 GHz (E2) and 22.6 GHz (E3) and are limited by device's self-heating and extrinsic parasitic resistance and capacitance.

To measure the RIN, the VCSEL devices are biased at constant currents. The laser output is collimated by an anti-reflection coated lens and focused into an optical fiber and received by a 25 GHz bandwidth photodetector. A free space optical isolator (isolation > 30 dB) is employed to reduce the laser back-reflection into the cavity. The fiber optical coupling efficiency is ~92%. The DC photocurrent is monitored by a digital multi-meter, and the separated AC signal is amplified by two cascaded amplifiers, each with a bandwidth of 13.5 GHz, a noise figure of 5.8 dB, and a power gain of 21 dB. The amplified system noise power spectrum, $N_{RF}(f)$ is measured by a signal analyzer with 13.6 GHz bandwidth. The thermal noise power spectrum $N_{th}(f)$ is measured by the same signal analyzer through turning off the laser and keeping the

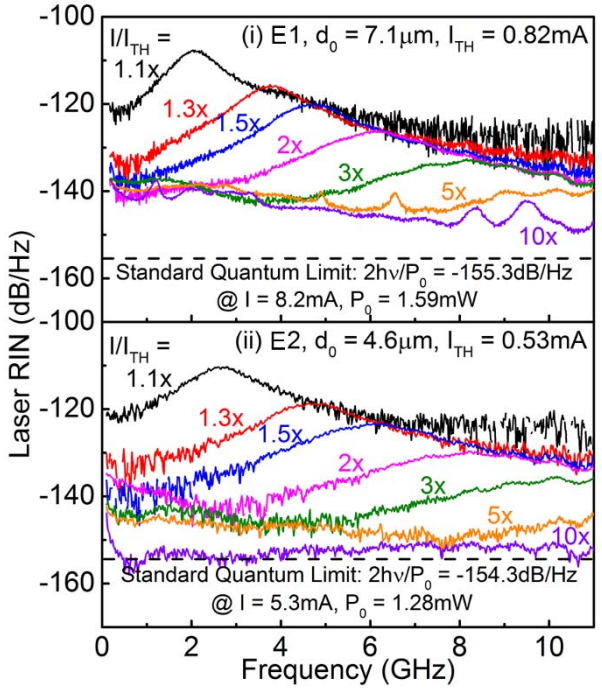

Fig. 4. Measured laser RIN of devices E1 and E2 for $I/I_{TH} = 1.1$ to 10. E1 shows higher RIN than the "standard quantum limit" at $I/I_{TH} = 10$ due to the mode partition noise and polarization fluctuation. In contrast, E2 shows the laser RIN saturates to the standard quantum limit, $2h\nu/P_0$.

operation of the photodetector and amplifiers. The intrinsic laser RIN can be extracted by removing the thermal noise and the photodetector shot noise from the system noise power spectrum

$$RIN|_{laser}(f) = \frac{N_L(f)}{P_{avg,elec}} = \frac{[N_{RF}(f) - N_{th}(f)]/G(f) - N_{PD,shot}}{P_{avg,elec}} \quad (8)$$

Here N_L is the electrical noise power spectral density induced by laser intensity noise. $N_{PD,shot} = 2qI_{dc}R_L$ and $P_{avg,elec} = (I_{dc})^2 R_L$ are the shot noise power spectral density and the electrical average power output of photodetector under the average input optical power P_0, respectively. R_L is the load resistance of the amplifier input port. $I_{dc} = rP_0$ and r are the output photocurrent and responsivity of the photodetector, respectively. Figure 4 shows the measured laser RIN of devices (a) E1 and (b) E2 for laser bias current $I/I_{TH} = 1.1$ - 10. For VCSEL DE1 ($d_0 = 7.1\ \mu$m), it shows higher laser RIN due to the large mode partition noise at high bias current I = 8.2 mA ($I/I_{TH} = 10$) with a laser output power $P_0 = 1.59$ mW. In addition, it shows several resonance peaks which may come from polarization fluctuation. For VCSEL E2 ($d_0 = 4.6\ \mu$m), the laser RIN reaches the standard quantum limit $2h\nu/P_0 = -154.3$ dB/Hz at high bias current I = 5.3 mA ($I/I_{TH} = 10$) with a laser output $P_0 = 1.28$ mW. The results indicate that the device with smaller optical modal dimension exhibits lower laser RIN, which is due to the less mode competition inside the smaller optical cavity volume.

Figure 5 shows the measured BER of E2 VCSEL ($d_0 = 4.6\ \mu$m) as a function of detected optical power under

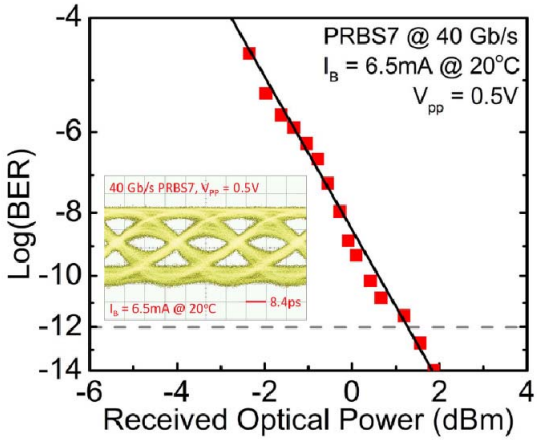

Fig. 5. Measured BER vs. received optical power of the E2 VCSEL device operating at 40 Gb/s with PRBS7 data sequence at 20 °C. The bias current is I = 6.5 mA, and the corresponding ac voltage swing amplitude is Vpp = 0.5 V. Inset is the Eye diagram of the VCSEL device operating at 40 Gb/s with PRBS7 data sequence.

the bias current of 6.5 mA at 20 °C, and the corresponding voltage swing amplitude is $V_{pp} = 0.5$ V. Error-free transmission (BER $< 10^{-12}$) is obtained at optical power P > 1.33 mW. At optical power P = 1.73 mW, it shows no error for more than 1 hour (total acquisition bits $> 1.5 \times 10^{14}$). Inset displays the eye diagram of the VCSEL operating at 40 Gb/s with PRBS7 data sequence. It shows a clear open-"eye" at 40 Gb/s. Based on the BER measurement results, we calculate the energy/data efficiency at 40 Gb/s for the 4 μm oxide aperture VCSEL device. The energy/data efficiency is defined as the power consumption $P_{elec} = I \cdot V$ of the device divided by the corresponding error-free data transmission rate. Thus, the energy/data efficiency is calculated to be 431 fJ/Bit.

C. Small-Signal Model and Microwave Extraction

In the following we discuss the microwave behavior of microcavity VCSELs. We use both the electrical (S_{11}) and optical (S_{21}) frequency response, which are measured by Parameter Network Analyzer (PNA), to estimate the enhanced recombination rate and reduced recombination lifetime inside a microcavity laser. To understand the electrical and optical behavior of the device, we start from the coupled carrier-photon rate equations, which were first formulated by Statz and deMars [81] in 1960,

$$\begin{cases} \dfrac{dN}{dt} = \dfrac{I_d}{q} - \dfrac{N}{\tau_{rec}} - gN_p \\ \dfrac{dN_p}{dt} = gN_p - \dfrac{N_p}{\tau_p} + \beta\dfrac{N}{\tau_{rec}} \end{cases} \quad (9)$$

Here N is the total carrier population inversion, N_p is the photon population inside the cavity, and I_d is the injection current. The quantity τ_{rec} ($\sim$ ns) is the carrier recombination lifetime, and τ_p ($\sim$ ps) is the photon lifetime inside the cavity. The expression $g = \Gamma v_g \alpha(N/V - n_0)$ is the effective optical gain, where Γ, v_g and α are the confinement factor, group velocity, and QW gain constant, respectively. The quantity V is the active region volume, and n_0 is the carrier density

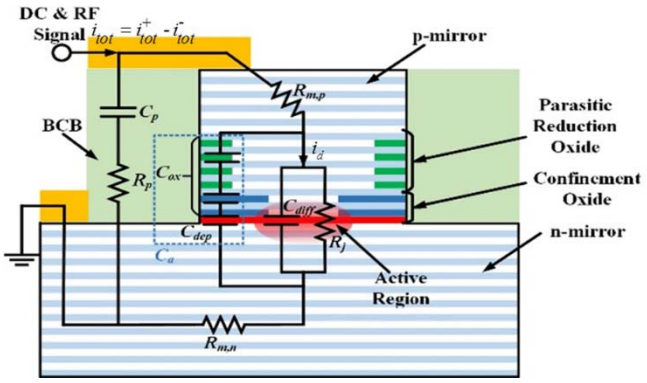

Fig. 6. Physical model with equivalent circuit including the parasitic parameter identified as follows: Cp and Rp, the p-pad capacitance and resistance; Rm,p and Rm,n, the p-DBR and n-DBR mirror series resistance; Cdiff, diffusion capacitance at the active region; Rj, junction resistance at the active region; Cox and Cdep, the lumped oxide capacitance and depletion capacitance. Ca is the total parasitic capacitance resulted from Cox and Cdep.

at transparency. Here β is a spontaneous emission coupling factor, indicating the fraction of photons (number) coupled into the cavity mode relative to the total number of photons. As the bias current extends beyond threshold, gain is clamped to the cavity loss $g = 1/\tau_p$, and the coherent field becomes self-sustaining. Injected carriers supply both the stimulated and spontaneous carrier recombination. By solving Eq. (9), we obtain the optical frequency response as a transfer function

$$S_{21,\text{int}}(f) = \frac{A}{1 - f^2/f_R^2 + j(f/2\pi f_R^2)\gamma} \tag{10}$$

Here A is magnitude fitting parameter, f_R is the resonance frequency, and γ is the damping factor which determines the oscillation relaxation. An approximation to the -3dB bandwidth is $f_{-3dB} \sim 1.55 \times f_R$. The intrinsic bandwidth of the optical response is determined by both the photon density, $N_p/V = (I - I_{TH})\tau_p/qV$, and the spontaneous recombination lifetime, τ_{rec}. The photon density N_p/V inside of the cavity determines the bandwidth of the response, and the recombination lifetime, τ_{rec}, influences the damping of the relaxation oscillations and the bandwidth.

When the optical mode volume becomes smaller and smaller, we excite fewer modes within the gain profile, resulting in the enhancement of the stimulated emission photon rate, gN_p, and lowering the threshold current. Hence, the intrinsic modulation speed for a microcavity laser can be improved. On the other hand, the microcavity can also enhance the spontaneous recombination rate $1/\tau_{rec}$ (by the Purcell effect), which increases the damping factor, yielding a smaller resonance peak and increased the bandwidth.

In order to obtain the intrinsic modulation bandwidth to then determine the recombination lifetime for a VCSEL based on the rate equations, we have to eliminate the parasitic contributions. Therefore, we construct the physical small-signal circuit model of VCSEL to model electrical parasitic parameters. The schematic cross section of the VCSEL with all the related extrinsic parasitic parameters is shown in Fig. 6 for the improved epitaxial structure. The physical meaning of each parameter is described in the annotation of Fig. 6.

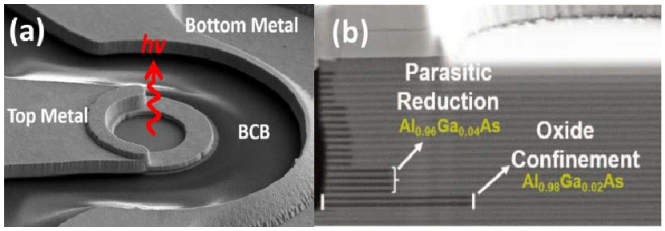

Fig. 7. (a) The SEM top view, and (b) the cross-section view of a oxide-confined VCSEL.

If the mirror resistance is partially attributed to terminate the output port, the reflection coefficient, $\Gamma(f)$, is equivalent to $S_{11}(f)$ and can be expressed as,

$$\Gamma(f) = S_{11} = \frac{i^-_{tot}(f)}{i^+_{tot}(f)} = \frac{i^+_{tot}(f) - i_{tot}(f)}{i^+_{tot}(f)}, \tag{11}$$

where $i^+_{tot}(f)$ is the transmitted modulation current wave and $i^-_{tot}(f)$ is the reflected modulation current wave. The total modulation current injected to the VCSEL at frequency f can be defined as $i_{tot}(f) = i^+_{tot}(f) - i^-_{tot}(f)$ at the input node. The electrical parasitic transfer function can be expressed as,

$$H_{par}(f) = \frac{i_d(f)}{i^+_d(f)} = \frac{i_d(f)}{i_{tot}(f)} \cdot (1 - S_{11}) \tag{12}$$

where $i_d(f)$ is the portion of the transmitted small signal modulation current that goes through the diode intrinsic active region. By fitting both the magnitude and the phase of the $S_{11}(f)$ measurement data, the electrical parasitic parameters can be extracted and be used to formulate the electrical parasitic transfer function.

Thus, the overall measured frequency modulation response can be expressed as the extrinsic optical response (i.e. electrical parasitics are included) in addition with the photodetector response:

$$\begin{aligned} S_{21,\text{overall}}(f) &= S_{21,\text{ext}}(f) \cdot H_{PD}(f) = \frac{N_p(f)}{i^+_{tot}(f)} \cdot H_{PD}(f) \\ &= \frac{i_d(f)}{i^+_{tot}(f)} \cdot \frac{N_p(f)}{i_d(f)} \cdot H_{PD}(f) \\ &= H_{par}(f) \cdot S_{21,\text{int}}(f) \cdot H_{PD}(f) \end{aligned} \tag{13}$$

From Eq. (13), the intrinsic optical response of Eq. (9) can be readily obtained by de-embedding electrical parasitic transfer function, $H_{par}(f)$, and photodetector transfer function, $H_{PD}(f)$, out of the measured optical response.

The microwave equivalent circuit model is developed based on the physical structure and epitaxial layering of the oxide-confined VCSEL. The 850 nm oxide-VCSEL material is grown by MOCVD and reported [20]. Figure 7 shows the SEM pictures of the top view of the as-fabricated VCSEL and cross–section of the top DBR mirror with lateral oxides.

The DC characteristics of the device, such as light-current-voltage (*L-I-V*) and optical emission spectrum, are shown before the discussion of equivalent circuit model and the microwave characteristics. The device is mounted on a temperature-controlled stage and probed with 50 GHz bandwidth ground-signal-ground (GSG) probes. The device under test is biased with DC current, and the optical light

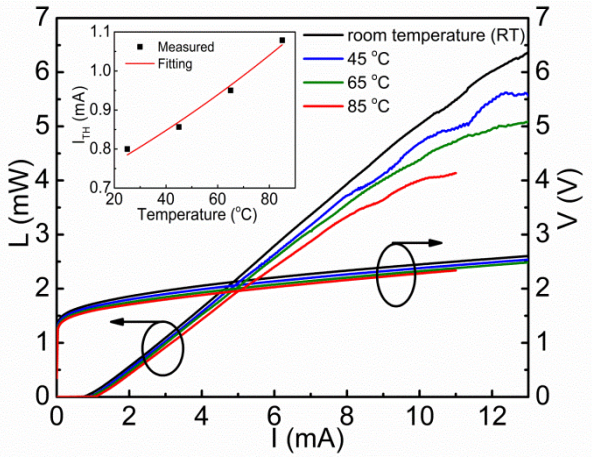

Fig. 8. L-I-V characteristics of the 850 nm oxide-confined VCSEL from room temperature (~25 °C) to 85 °C. The inset shows the measured data and fitting of the threshold current versus temperature to obtain I_o = 0.69 mA and T_o = 195 °C.

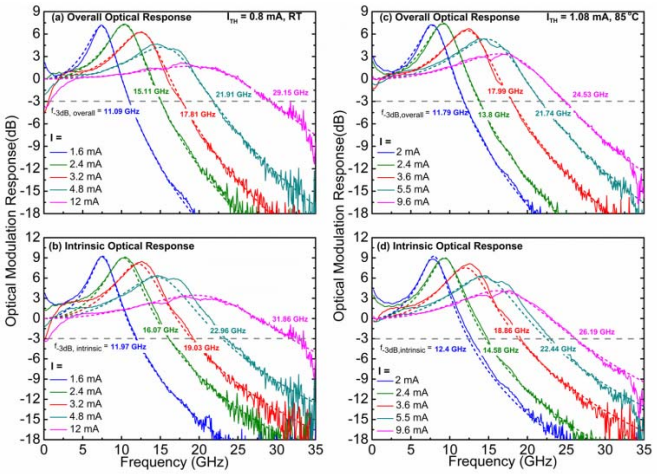

Fig. 9. (a) & (c) The overall optical frequency response of the 5 μm optical aperture VCSEL at RT and 85 °C. (b) & (d) The intrinsic optical response of the 5 μm optical aperture VCSEL. The highest −3 dB modulation bandwidth of the overall optical response is 29.15 GHz and 24.53 GHz at RT and 85 °C whereas it is 31.86 GHz and 26.19 GHz for the intrinsic optical response at RT and 85 °C.

output is collimated and coupled into a 50 μm core diameter OM4 MMF through a lens package constructed with anti-reflection (AR) coating. The temperature-dependent, from 25 to 85 °C, light-current-voltage (*L-I-V*) characteristics of the device are shown in Fig. 9. The threshold current increases from I_{TH} = 0.8 mA at 25 °C to 0.86 mA at 45 °C, to 0.95 mA at 65 °C, and finally to 1.08 mA at 85 °C. The fitted data of threshold current with respect to temperature for the VCSEL is shown in the inset of Fig. 8, and the fitted 0 °C threshold current and characteristics temperature are I_o = 0.69 mA and T_o = 195 °C respectively. Derived from the slope of the L-I curves, the slope efficiency of the device is ~ 0.58 W/A at room temperature and ~ 0.5 W/A at 85 °C.

The intrinsic laser optical response, $S_{21,int}(f)$, can be fitted by de-embedding measured $S_{21,\,overall}(f)$ at various biasing current points over the frequency range of 0.1 to 35 GHz. Figure 9 (a) to (d) shows the overall and intrinsic small signal optical modulation response of the modeled VCSEL at various biasing points at both RT and 85 °C.

The damping rate, γ, in this context is related to ability of the VCSEL device to convert carriers into photons. If the carrier injection rate is faster than the electron-to-photon conversion rate, excess carrier concentration in the QWs will build up and "choke" the optical modulation response as indicated from the laser resonant frequency effect shown in Figure 9. At higher I/I_{TH}, the cavity optical field intensity increases and expedites the stimulated recombination process, and hence the carrier choking effect reduces and resonance peak amplitude decreases.

We can fit the intrinsic optical bandwidth with the two-pole laser transfer function shown in Eq. (9) with the parameters, f_R and γ, to estimate both the recombination lifetime, $\tau_{\rm rec}$, and photon lifetime, $\tau_{\rm p}$, by using the following equations.

$$f_R = \frac{1}{2\pi}\sqrt{\frac{v_g g'}{qV_p}\eta_i(I - I_{TH})} = \frac{1}{2\pi}\sqrt{\frac{g' N_{TH}}{g_{TH}} \cdot \frac{1}{\tau_{rec}\tau_p}(I/I_{TH} - 1)} \quad (14)$$

$$\gamma = Kf_R^2 + \frac{1}{\tau_{rec}} \cong 4\pi^2\tau_p f_R^2 + \frac{1}{\tau_{rec}} \quad (15)$$

where

$$K = 4\pi^2\tau_p\left[1 - \Gamma\frac{\partial N}{\partial N_p}\right] \approx 4\pi^2\tau_p \quad (16)$$

The K-factor, K, relates the damping rate, γ to the resonance frequency, f_R. By plotting the microwave modelling of γ against f_R^2, the photon lifetime, τ_p, and recombination lifetime, τ_{rec}, can be extracted. Two assumptions were made so the estimated value of τ_p can be extracted from the modelling data. According to Eq. (16), the K-factor is also dependent on Γ, the optical confinement factor, and $\frac{\partial N}{\partial N_p}$. The assumption that the optical modal volume, V_p, is larger than the electrical carrier injection volume, V, in the active region is made so the confinement factor, $\Gamma = V/V_p$, is negligible. Furthermore, the assumption that the change of carriers in the active region is comparable to the change of photons is made and therefore, $\frac{\partial N}{\partial N_p} \cong 1$. With these two assumptions, the approximation in Eq. (16) is reached.

Figure 10 shows the plot of γ vs. f_R^2. From the intercept and the linear slope, we can determine the K-factor, the photon lifetime, and the recombination lifetime of the VCSEL according to Eqns. (14)-(16). The extracted recombination and photon lifetimes at RT, 45 °C, 65 °C and 85 °C are summarized in the inset table of Fig. 10 Both of the recombination and photon lifetimes increase as temperature increases from RT to 85 °C. The increase of recombination lifetime is expected. As temperature increases, the carriers on average have higher thermal *KT* energy and therefore there is a higher chance for carriers to either skip through the quantum wells without being captured or escape out of the quantum well after being captured. These physical phenomena will, hence, result in higher recombination lifetime.

The photon lifetime is related to photon loss rate out of the optical cavity; longer photon lifetime at higher temperature

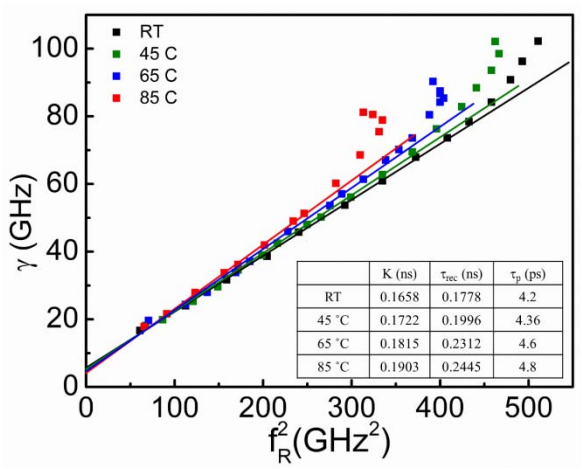

Fig. 10. Fitted damping rate, γ vs. fitted resonance frequency squared, f_R^2, at RT, 45, 65 and 85 °C. The extracted K-factor, recombination lifetime, τ_{rec}, and photon lifetime, τ_p, are listed in the inset table.

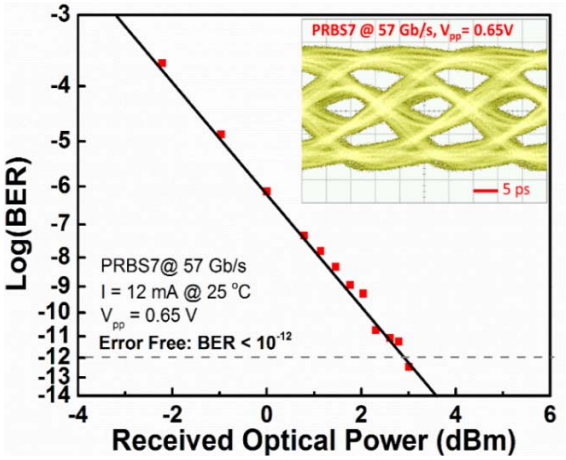

Fig. 11. The 57 Gb/s bit-error rate (BER) vs. received optical power of the oxide-VCSEL biased at 12 mA. The inset shows the eye diagram at 57 Gb/s.

indicates less photon loss. The lower photon loss rate can be attributed to the reduction of material absorption (α_i) and the decrease of the mirror loss (α_m). In this case, the decrease of the mirror loss is related to the increase of the contrast of refractive index of the p-DBR stack. The decrease of refractive index in high Al content of $Al_{0.9}Ga_{0.1}As$ layers at higher temperature can be attributed to more thermally induced carriers from the deep and interface trap levels contributing to a higher hole concentration [82], [83]. Therefore, the contrast of refractive index between the high/low content $Al_xGa_{1-x}As$ layers increases.

The effect of thermally induced increase of carrier concentration in the low Al content can be neglected as deep level concentration is insignificant for Al content below 0.3 [84]. Therefore, it can be assumed that only the refractive index of the high Al content decreases, leading to a larger contrast of refractive indexes between the alternating Al content p-DBR mirror layers. Resulting from the further refractive index contrast, the optical cavity provides a better photon confinement, Q factor, and hence the average time that takes a photon to leave the p-DBR mirror stack, τ_p, increases.

D. Oxide-Confined VCSELs With > 50 Gb/s Error-Free Transmission Up to 85 °C Operation

In this section, the bit error ratio test (BERT) results and the corresponding eye diagrams at the data transmission rate are shown at both RT and 85 °C. The transmission interconnect setup consists of a SHF 12103A Bit Pattern Generator (BPG) that provides the modulation bit sequence, the same light collimation module used for DC and RF measurement, a 2 m OM4 optical fiber that collects the coupled light from the light collimation module and a New Focus 1484-A-50 22 GHz high-gain photoreceiver that converts the collected optical signal back into electrical signal. The test bit sequence used is an non-return-to-zero (NRZ) $2^7 - 1$ pseudorandom binay sequence (PRBS7) with a peak-to-peak voltage swing $V_{pp} = 0.65$ V generated by the SHF BPG. An Agilent Oscilloscope with 70 GHz bandwidth sampling module is used to capture the eye diagrams. To validate the transmission performance of the device, the converted electrical signal from the photoreceiver is sent to the SHF 11104A Error Analyzer for BER testing. A free space neutral density filter is used to attenuate the received optical power into the optical fiber to characterize the BER as a function of optical power.

The VCSEL shows a threshold of $I_{TH} = 0.8$ mA and slope efficiency of 0.58 W/A at RT as shown in Fig. 8. The optical modal diameter, d_o, is estimated to be 5 μm. Figure 11 shows the BER measurement at a data rate of 57 Gb/s when the device is biased at 12 mA, and the corresponding differential resistance from the I-V characteristics is ~53 Ω. For received optical power greater than 1.96 mW, the oxide-VCSEL is able to show error-free (BER $<10^{-12}$) transmission. Because of the better impedance match to the standard 50 Ω testing system, our device does not require extra amplification on the test bit sequence to pass the BER test. The inset of Fig. 11 shows the eye diagram at 57 Gb/s, and the device is able to show an "open"-eye when biased at I = 12 mA. The energy/data efficiency, $P_{electrical}$/Error-Free Data Rate, is 539 fJ/bit.

Figure 12 (a) shows eye diagrams at 85 °C with the data rate of 46 and 50 Gb/s of the device biased at I = 10 mA. Figure 15 (b) shows the BER measurement, and the device is able to demonstrate error-free (BER $< 10^{-12}$) transmission at 46 and 50 Gb/s at received optical power greater than 0.54 and 1.95 mW, respectively at 85 °C. The power penalty is therefore 5.6 dBm when the data rate increases from 46 Gb/s to 50 Gb/s. Previously reported data on a single device 850 nm oxide-confined VCSEL, without using equalization, has shown error-free transmission at 40 Gb/s up to 85 °C [13] and 50 Gb/s up to 57 °C [78]. This reported 50 Gb/s error-free transmission oxide VCSEL is the highest speed to date for any 850 nm oxide-confined VCSEL at 85 °C without the uses of equalization.

At the bias I = 10 mA at 85 °C, the device's differential resistance is ~ 58 Ω, derived from the I-V characteristics. Due to the better impedance match to standard 50 Ω of testing instruments, no external amplification was implemented to

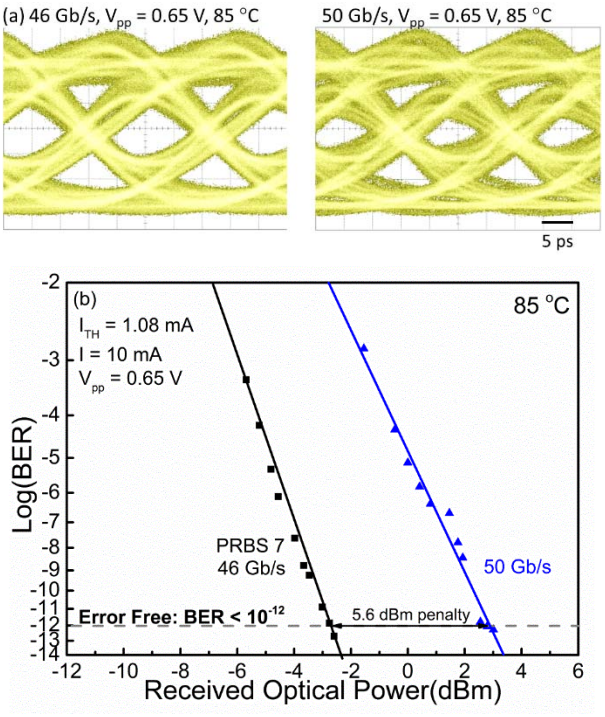

Fig. 12. (a) Eye diagrams at 46 Gb/s and 50 Gb/s under the bias of I = 10 mA and V_{pp} = 0.65 V at 85 °C for the 5 μm optical aperture VCSEL. (b) BER (46 Gb/s and 50 Gb/s) versus received optical power for the optical link based on the 5 μm optical aperture VCSEL at 85 °C. The power penalty is 5.6 dBm when the data rate increases from 46 Gb/s to 50 Gb/s under the same biasing condition.

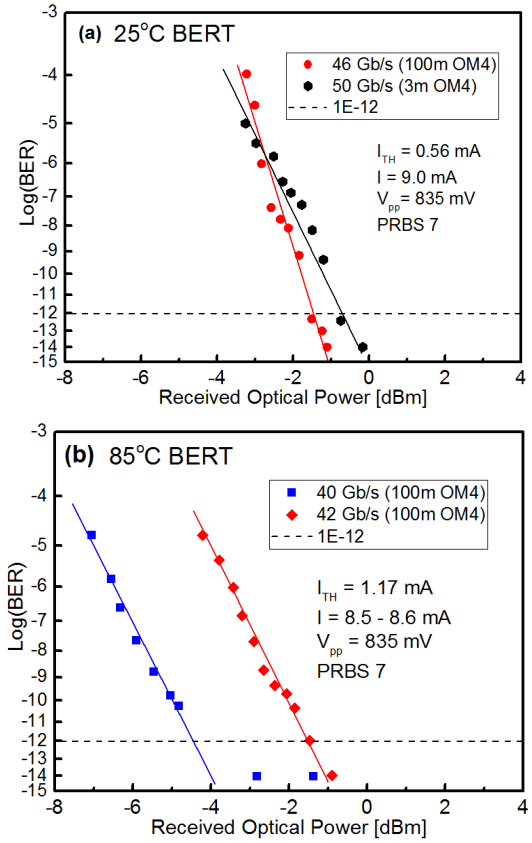

Fig. 13. (a) 50 Gb/s and 46 Gb/s BER versus received optical power at 25°C and (a) 42 Gb/s BER versus received optical power at 85°C.

acquire the error-free transmission results. Higher speed error-free transmission could possibly be achieved if amplifications were utilized. The energy/data efficiency at 50 Gb/s is calculated 456 fJ/bit at 85 °C.

E. Oxide-Confined VCSELs With 42 Gb/s Error-Free Transmission Up to 85 °C Over 100 Meter OM4 Link

For data transmission over fibers, the modal dispersion in fibers will need to be maintained. For the 100 meter OM4 MMF links, 850 nm VCSELs have previously been reported of 43 Gb/s at 25°C [11]. Here we continue to reduce the leakage current and control the microcavity modes of VCSELs. The 3dB modulation bandwidth after de-embedding the photodetector response is 25 GHz at room temperate and 21 GHz at 85°C, respectively.

The BERT results are shown in Fig. 13. The test bit sequence used is non-return-to-zero 2^7-1 bit length pseudo-random binary series (PRBS 7) with a peak-to-peak AC voltage swing V_{pp} = 835 mV generated by a SHF Bit Pattern Generator followed by a 7 dB power amplifier. The oxide-confined VCSELs have demonstrated room temperature 50 Gb/s error-free data transmission on a 3 meter link (BTB) and record performance of 46 Gb/s on 100 meter link with received optical power ~0.70 mW as shown in Fig. 17(a). The devices have achieved record speed of 42 Gb/s at 85°C on a 100 meter OM4 link with received optical power ~0.80 mW as shown in Fig. 13(b). A 3-dB power penalty from 40 Gb/s to 42 Gb/s determined from experimental data fitting is reported. Because the devices reach the thermal limited light output at the bias current closed to 9 mA, the V_{pp} of 835 mV has been set from Bit Pattern Generator to improve the signal to noise ratio of measurement. From the electrical power consumption of the device, we obtained device energy per bit of ~460 fJ/bit at 42 Gb/s at 85°C for a100 meter OM4 link. In summary, we demonstrate the error-free data transmission for a 100 meter MMF link with a record data rate of 46 Gb/s at 25°C, 43 Gb/s at 75°C, and 42 Gb/s at 85°C without the use of signal processing such as equalizer or forward error correction.

Figure 14 summarizes the record performance of 850 nm VCSELs' NRZ error-free data rate (> 30 Gb/s) transmission versus operating temperature (25 to 85°C) for BTB, 50, and 100 meter links. The VCSEL performance can be further enhanced with better heat dissipation to improve the thermal limitation at the current bias point.

F. Back-to-back 16-QAM OFDM Transmission With 850-nm Oxide-Confined VCSEL at 104 Gbit/s

To increase the data allocation efficiency with highly spectral usage for enabling large transmission capacity, the orthogonal frequency-division multiplexed M-array quadrature-amplitude modulation (M-QAM OFDM) has also been considered as the solution [85]–[87]. In the following work, the 850-nm oxide-confined VCSELs modulated directly

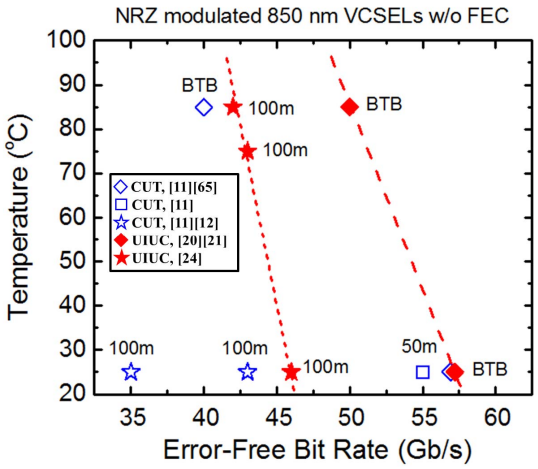

Fig. 14. 850 nm VCSELs NRZ modulated error-free bit rate transmission for different MMF link distance versus temperature from 25 to 85°C.

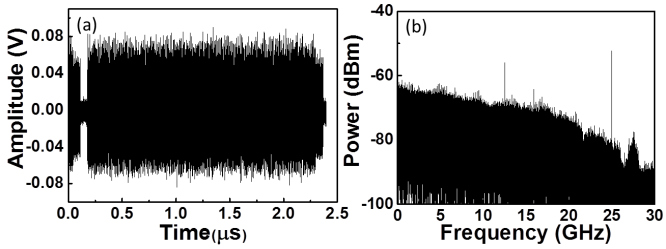

Fig. 15. (a) The waveform in time domain, and (b) the spectrum in frequency domain of the received 16-QAM OFDM data stream without OFDM amplitude pre-leveling.

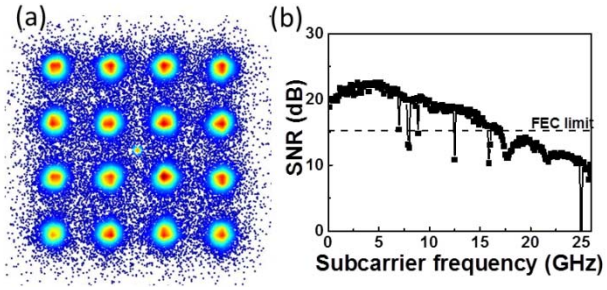

Fig. 16. (a) The constellation plot, and (b) the SNR spectrum of the un-pre-leveled 16-QAM OFDM data carried by the few-mode VCSEL chip.

with the 16-QAM OFDM data is achieved with a raw data rate of 104 Gbit/s through BTB transmission. After optimizing the error vector magnitude (EVM), SNR, and BER with bias current adjustment, the amplitudes of OFDM subcarriers at different frequencies are also pre-leveled to improve the transmission data rate.

The file of a 16-QAM OFDM data is generated from a homemade MATLAB program, which is fed into the arbitrary waveform generator (AWG, Keysight M8195A) for delivering the QAM OFDM waveform. The oxide-VCSEL is directly modulated with combining the 16-QAM OFDM data and the DC bias current via a bias-tee. The DC bias is set as 6 mA and the peak-to-peak data amplitude is set as 1.0 volt. The temperature of the oxide-VCSEL is controlled at 25°C. The lensed multi-mode fiber is employed to couple the VCSEL output into a 22-GHz photodetector (PD, New Focus 1484-A-50) at receiving end. After capturing the received waveform by a real-time digital serial analyzer (DSA, Tektronix DPO77002SX) with 100-GS/s sampling rate, the QAM OFDM data is off-line demodulated with an in-house developed MATLAB code to analyze the transmission performance including EVM, SNR, and BER.

The VCSEL is biased to suppress its relative-intensity-noise to −134 dBc/Hz within modulation bandwidth, which provides 1.6-mW output at a differential resistance of 70 Ω. The highest modulation bandwidth and the lowest RIN level of the VCSEL guarantee the broadband QAM-OFDM modulation and transmission with sufficiently high SNR after receiving and decoding. The key parameters can be optimized by the bias current to provide higher throughput power, better impedance matching, large modulation bandwidth and lower noise level. After optimization, the waveform and the Fourier transformed spectrum of the received 16-QAM OFDM data is shown in Fig. 15, which reveals a two-step throughput power declination with power-to-frequency slope of −0.3 dB/GHz the allocated data from DC to17 GHz and −1.0 dB/GHz for the allocated data from 17 GHz to 26 GHz.

Figure 16 plots the constellation plot and the SNR response of the received 16-QAM OFDM data carried by the 850 nm VCSEL, which presents an EVM of 18.7% and an average SNR of only 14.5 dB within the modulation data bandwidth of 26 GHz. Some of the data carried by the OFDM subcarriers at frequency below 17 GHz can successfully exceed the required SNR of 15.2 dB, whereas others at higher OFDM subcarrier frequencies gives the SNR of lower than 14 dB. This results in a total receiving BER of 6.3×10^{-3} and fails to meet the FEC criterion.

Owing to the limitation on the total output power from the arbitrary waveform generator, the spectral amplitudes of the QAM data carried by the high-frequency OFDM subcarriers can be rearranged to "pre-emphasize" the high-frequency response, which can compensate the declination of modulation throughput due to the finite bandwidth of the VCSEL. With subcarrier pre-leveling, the received 16-QAM OFDM data waveform delivered by the oxide-confined VCSEL shows less fluctuated envelope than the case without pre-leveling. Nevertheless, the peak-to-peak amplitude of the received waveform is somewhat attenuated due to the rearrangement on the OFDM subcarrier amplitude at different frequencies. Indeed, the Fourier transformed data spectrum shows a less declined throughput power as compared to that without pre-leveling. Figure 17 declares that the power-to-frequency declination slope of the 16-QAM data has already suppressed to −0.26 dB/GHz at OFDM subcarrier frequency below 17 GHz and −1.1 dB/GHz at OFDM subcarrier frequency ranged between 17 GHz and 26 GHz.

After decoding the pre-leveled 16-QAM OFDM data carried by the oxide-confined VCSEL, the constellation plot shown in Fig. 18 reveals a clearer pattern than that decoded from the un-pre-leveled data. In contrast to the received data without OFDM subcarrier amplitude pre-leveling, the EVM is determined as small as 17.3%, and the undecodable data accumulated in the central part of the constellation plot

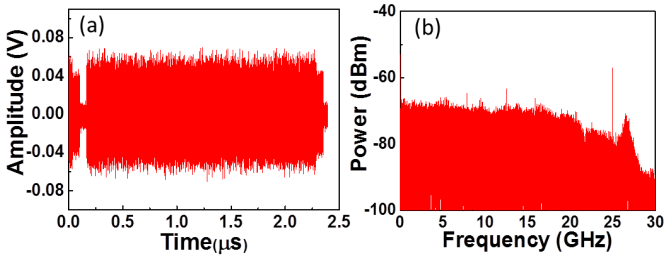

Fig. 17. (a) The waveform in time domain, and (b) the spectrum in frequency domain of the received 16-QAM OFDM data stream with pre-leveling the OFDM amplitude.

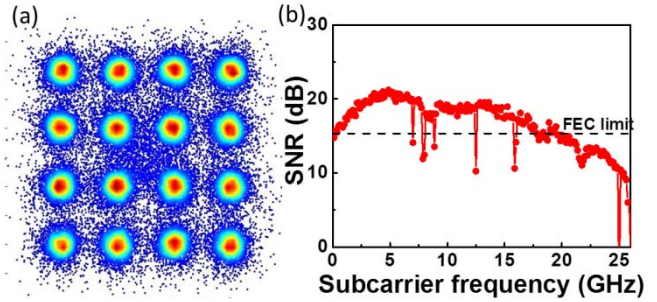

Fig. 18. (a) The constellation plot, and (b) the SNR spectrum of the pre-leveled 16-QAM OFDM data carried by the few-mode VCSEL chip.

disappears. The SNR of the 16-QAM data carried by different OFDM subcarriers within the modulation bandwidth also shows an enhancement at higher frequencies by slightly sacrificing the data power carried at lower OFDM subcarrier frequencies. Such a pre-emphasis technique effectively optimizes the average to 15.2 dB. This results in a total receiving BER of 3.8×10^{-3}, and passes the FEC criterion.

IV. Conclusion

The oxidation process invented at Illinois has led to commercial success of VCSELs in optical interconnects for data communication. Through the reduction of oxide-confined apertures, the optical mode can be tailored to reduce the recombination lifetime and enhance the modulation bandwidth. A thermal-noise-limited laser intensity noise exhibits the low power operation and reduced mode competition of the microcavity VCSEL. A better signal transmission integrity can also be achieved in the microcavity VCSELs. We use microwave measurement to construct small-signal circuit model to analyze the electrical-to-optical response and resolve the dynamics of carrier-photon interaction at different temperatures. We present 57 Gb/s error-free transmission at room temperature, and up to 50 Gb/s data rate at 85 °C. By reducing the threshold current and optical mode volume, transmission rates over 100 m OM4 fiber can be up to 46 Gb/s at room temperature, and 42 Gb/s at 85 °C without the use of equalizers. Finally, the pre-leveled 16-QAM OFDM data at a raw data rate of 104 Gbit/s under back-to-back transmission shows the received EVM, SNR, and BER of 17.3%, 15.2 dB, and 3.8×10^{-3}, respectively.

Acknowledgement

The authors would like to thank the key contributions from Dr. Han Wui Then (Intel), Dr. Fei Tan (Apple), Dr. Mong-Kai Wu (Intel), Dr. Michael Liu (Intel), Mr. Curtis Y. Wang, Mr. Junyi Qiu, Mr. Hsiao Lung Wang and Dr. Xin Yu. We are grateful for the support from Prof. Gong-Ru Lin from National Taiwan University and his graduate student Mr. Cheng-Yi Huang and Mr. Huai-Yung Wang on oxide-confined VCSEL based OFDM measurement and analysis.

References

[1] H. W. Then, C. H. Wu, M. Feng, and N. Holonyak, Jr., "Microwave characterization of Purcell enhancement in a microcavity laser," *Appl. Phys. Lett.*, vol. 96, no. 13, 2010, Art. no. 131107.

[2] C. H. Wu, H. W. Then, M. Feng, and N. Holonyak, "Microwave determination of electron-hole recombination dynamics from spontaneous to stimulated emission in a quantum-well microcavity laser," *Appl. Phys. Lett.*, vol. 96, no. 13, 2010, Art. no. 131108.

[3] C. H. Wu, F. Tan, M. Feng, and N. Holonyak, Jr., "The effect of mode spacing on the speed of quantum-well microcavity lasers," *Appl. Phys. Lett.*, vol. 97, no. 9, 2010, Art. no. 091103.

[4] C. H. Wu, F. Tan, M. Feng, and N. Holonyak, "The effect of microcavity laser recombination lifetime on microwave bandwidth and eye-diagram signal integrity," *J. Appl. Phys.*, vol. 109, no. 5, 2011, Art. no. 053112.

[5] F. Tan, C. H. Wu, M. Feng, and N. Holonyak, Jr., "Energy efficient microcavity lasers with 20 and 40 Gb/s data transmission," *Appl. Phys. Lett.*, vol. , vol. 98, no. 19, 2011, Art. no. 191107.

[6] F. Tan, M. K. Wu, M. Liu, M. Feng, and N. Holonyak, Jr., "Relative intensity noise in high speed microcavity laser," *Appl. Phys. Lett.*, vol. 103, no. 14, 2013, Art. no. 141116.

[7] F. Tan, M. K. Wu, M. Liu, M. Feng, and N. Holonyak, "850 nm oxide-VCSEL with low relative intensity noise and 40 Gb/s error free data transmission," *IEEE Photon. Technol. Lett.*, vol. 26, no. 3, pp. 289–292, Feb. 1, 2014.

[8] M. Liu, M. K. Wu, and M. Feng, "Optimization of selective oxidation for 850 nm (IR) and 780 nm (far-red) energy/data efficient oxide-confined microcavity VCSELs," in *Proc. Compound Semicond. Manuf. Technol. Conf. (CSMANTECH)*, 2014, pp. 19–22.

[9] M. Liu, M.-K. Wu, F. Tan, R. Bambery, M. Feng, and N. Holonyak, "780 nm oxide-confined VCSEL with 13.5 Gb/s error-free data transmission," *IEEE Photon. Technol. Lett.*, vol. 26, no. 7, pp. 702–705, Apr. 1, 2014.

[10] F. Tan, M.-K. Wu, C. Wang, M. Liu, M. Feng, and N. Holonyak, "Effect of microcavity size to the RIN and 40 Gb/s data transmission performance of high speed VCSELs," in *Proc. Conf. Lasers Electro-Opt.*, San Jose, CA, USA, May 2015, p. SF1I.6.

[11] P. Westbergh, E. P. Haglund, E. Haglund, R. Safaisini, J. S. Gustavsso, and A. Larsson, "High-speed 850 nm VCSELs operating error free up to 57 Gbit/s," *Electron. Lett.*, vol. 49, no. 16, pp. 1021–1023, Aug. 2013.

[12] P. Westbergh *et al.*, "40 Gbit/s error-free operation of oxide-confined 850 nm VCSEL," *Electron. Lett.*, vol. 46, no. 14, pp. 1014–1016, Jul. 2010.

[13] P. Wolf, P. Moser, G. Larisch, H. Li, J. A. Lott, and D. Bimberg, "Energy efficient 40 Gbit/s transmission with 850 nm VCSELs at 108 fJ/bit dissipated heat," *Electron. Lett.*, vol. 49, no. 10, pp. 666–667, May 2013.

[14] P. Westbergh *et al.*, "High-speed oxide confined 850-nm VCSELs operating error-free at 40 Gb/s up to 85 °C," *IEEE Photon. Technol. Lett.*, vol. 25, no. 8, pp. 768–771, Apr. 15, 2013.

[15] P. Westbergh *et al.*, "High-speed 850 nm VCSELs with 28 GHz modulation bandwidth operating error-free up to 44 Gbit/s," *Electron. Lett.*, vol. 48, no. 18, pp. 1145–1147, Aug. 2012.

[16] E. Haglund *et al.*, "30 GHz bandwidth 850 nm VCSEL with sub-100 fJ/bit energy dissipation at 25–50 Gbit/s," *Electron. Lett.*, vol. 51, no. 14, pp. 1096–1098, Jul. 2015.

[17] M. Liu, C. Y. Wang, M. Feng, and N. Holonyak, "50 Gb/s error-free data transmission of 850 nm oxide-confined VCSELs," in *Proc. Opt. Fiber Commun. Conf.*, Anaheim, CA, USA, Mar. 2016, pp. 1–3.

[18] M. Liu, C. Y. Wang, M. Feng, and N. Holonyak, "850 nm oxide-confined VCSELs with 50 Gb/s error-free transmission operating up to 85 °C," in *Proc. Conf. Lasers Electro-Opt.*, San Jose, CA, USA, Jun. 2016, pp. 1–2, paper SF1L.6.

[19] M. Liu, C. Y. Wang, M. Feng, and N. Holonyak, "Advanced development of 850 nm oxide-confined VCSELs with 57 Gb/s error-free data transmission," in *Proc. GOMACTech*, Orlando, FL, USA, 2016, paper 27.4.

[20] C. Y. Wang, M. Liu, M. Feng, and N. Holonyak, Jr., "Microwave extraction method of radiative recombination and photon lifetimes up to 85 °C on 50 Gb/s oxide-vertical cavity surface emitting laser," *J. Appl. Phys.*, vol. 120, no. 22, 2016, Art. no. 223103.

[21] C. Y. Wang, M. Liu, M. Feng, and N. Holonyak, "Temperature dependent analysis of 50 Gb/s oxide-confined VCSELs," in *Proc. Opt. Fiber Commun. Conf. Exhib.,* Los Angeles, CA, USA, Mar. 2017, paper Tu3C.2.

[22] H. Wang, J. Qiu, X. Yu, M. Feng, and N. Holonyak, Jr., "85 °C Operation of 850 nm VCSELs deliver a 42 Gb/s error-free data transmission for 100 meter MMF Link," in *Proc. Opt. Fiber Commun. Conf. (OFC)*, San Diego, CA, USA, Mar. 2018, paper W1I.6.

[23] R. N. Hall, G. E. Fenner, J. D. Kingsley, T. J. Soltys, and R. O. Carlson, "Coherent light emission from GaAs junctions," *Phys. Rev. Lett.*, vol. 9, no. 9, p. 366, 1962.

[24] N. Holonyak, Jr., and S. F. Bevacqua, "Coherent (VISIBLE) light emission from $Ga(As_{1-x}P_x)$ junctions," *Appl. Phys. Lett.*, vol. 1, no. 4, pp. 82–83, 1962.

[25] I. Hayashi, M. B. Panish, P. W. Foy, and S. Sumski, "Junction lasers which operate continuously at room temperature," *Appl. Phys. Lett.*, vol. 17, no. 3, pp. 109–111, 1970.

[26] Z. I. Alferov *et al.*, "Investigation of the influence of the AlAs–GaAs heterostructure parameters on the laser threshold current and the realization of continuous emission at room temperature," *Fiz. Tekh. Poluprovodn.*, vol. 4, pp. 1826–1829, May 1970.

[27] E. A. Rezek *et al.*, "LPE $In_{1-x}Ga_xP_{1-z}As_z$ ($x \sim 0.12$, $z \sim 0.26$) DH laser with multiple thin-layer (<500 Å) active region," *Appl. Phys. Lett.*, vol. 31, no. 4, pp. 288–290, 1977.

[28] N. Holonyak, Jr., R. M. Kolbas, R. D. Dupuis, and P. D. Dapkus, "Room-temperature continuous operation of photopumped MO-CVD $Al_xGa_{1-x}As$-GaAs-$AlxGa_{1-x}As$ quantum-well lasers," *Appl. Phys. Lett.*, vol. 33, no. 1, pp. 73–75 1978.

[29] N. G. Basov, O. V. Bogdankevich, and A. G. Devyatkov, "Exciting of a semiconductor quantum generator with a fast electron beam," *Sov. Phys. Dokl.*, vol. 9, p. 288, Oct. 1964.

[30] I. Melngailis, "Longitudinal injection-plasma laser of InSb," *Appl. Phys. Lett.*, vol. 6, pp. 59–60, Feb. 1965.

[31] G. E. Stillman, M. D. Sirkis, J. A. Rossi, M. R. Johnson, and N. Holonyak, Jr., "Volume excitation, of an ultrathin single-mode CdSe laser," *Appl. Phys. Lett.*, vol. 9, no. 7, pp. 268–269, 1966.

[32] H. Soda, K.-I. Iga, C. Kitahara, and Y. Suematsu, "GaInAsP/InP surface emitting injection lasers," *Jpn. J. Appl. Phys.*, vol. 18, no. 12, pp. 2329–2330, 1979.

[33] K. Iga, S. Ishikawa, S. Ohkouchi, and T. Nishimura, "Room-temperature pulsed oscillation of GaAlAs/GaAs surface emitting injection laser," *Appl. Phys. Lett.*, vol. 45, no. 4, pp. 348–350, Aug. 1984.

[34] A. Ibaraki, S. Ishikawa, S. Ohkouchi, and K. Iga, "Pulsed oscillation of GaAlAs/GaAs surface-emitting injection laser," *Electron. Lett.*, vol. 20, no. 10, pp. 420–422, May 1984.

[35] F. Koyama, S. Kinoshita, and K. Iga, "Room-temperature continuous wave lasing characteristics of a GaAs vertical cavity surface-emitting laser," *Appl. Phys. Lett.*, vol. 55, no. 3, pp. 221–222, Jul. 1989.

[36] A. Ibaraki, K. Kawashima, K. Furusawa, T. Ishikawa, T. Yamaguchi, and T. Niina, "Buried heterostructure GaAs/GaAlAs distributed Bragg reflector surface emitting laser with very low threshold (5.2 mA) under room temperature CW conditions," *Jpn. J. Appl. Phys.*, vol. 28, no. 4, p. L667, 1989.

[37] H. Uenohara, F. Koyama, and K. Iga, "AlGaAs/GaAs multiquantum-well (MQW) surface-emitting laser," *Electron. Lett.*, vol. 25, no. 12, pp. 770–771, Jun. 1989.

[38] J. P. van der Ziel and M. Ilegems, "Multilayer GaAs-$Al_{0.3}Ga_{0.7}As$ dielectric quarter wave stacks grown by molecular beam epitaxy," *Appl. Opt.*, vol. 14, no. 11, pp. 2627–2630, 1975.

[39] M. Ogura, T. Hata, N. J. Kawai, and T. Yao, "GaAs/$Al_xGa_{1-x}As$ multilayer reflector for surface emitting laser diode," *Jpn. J. Appl. Phys.*, vol. 22, no. 1, p. L112, 1983.

[40] M. Ogura *et al.*, "Surface-emitting laser diode with vertical GaAs/GaAlAs quarter-wavelength multilayers and lateral buried heterostructure," *Appl. Phys. Lett.*, vol. 51, no. 21, pp. 1655–1657, 1987.

[41] T. Sakaguchi, F. Koyama, and K. Iga, "Vertical cavity surface-emitting laser with an AlGaAs/AlAs Bragg reflector," *Electron. Lett.*, vol. 24, no. 15, pp. 928–929, Jul. 1988.

[42] Y. H. Lee, J. L. Jewell, A. Scherer, S. L. McCall, J. P. Harbison, and L. T. Florez, "Room-temperature continuous-wave vertical-cavity single-quantum-well microlaser diodes," *Electron. Lett.*, vol. 25, no. 20, pp. 1377–1378, Sep. 1989.

[43] J. L. Jewell *et al.*, "Low-threshold electrically pumped vertical-cavity surface-emitting microlasers," *Electron. Lett.*, vol. 25, no. 17, pp. 1123–1124, Aug. 1989.

[44] J. M. Dallesasse, N. Holonyak, A. R. Sugg, T. A. Richard, and N. El-Zein, "Hydrolyzation oxidation of $Al_xGa_{1-x}As$-AlAs-GaAs quantum well heterostructures and superlattices," *Appl. Phys. Lett.*, vol. 57, no.26, pp. 2844–2846, 1990.

[45] J. M. Dallesasse and N. Holonyak, "Native-oxide stripe-geometry $Al_xGa_{1-x}As$-GaAs quantum well heterostructure lasers," *Appl. Phys. Lett.*, vol. 58, no. 4, pp. 394–396, 1991.

[46] J. M. Dallesasse *et al.*, "Native-oxide-defined coupled-stripe $Al_xGa_{1-x}As$-GaAs quantum-well heterostructure lasers," *Appl. Phys. Lett.*, vol. 58, no. 8, pp. 834–836, 1991.

[47] S. A. Maranowski, A. R. Sugg, E. I. Chen, and N. Holonyak, "Native oxide top- and bottom-confined narrow stripe $p-n$ $Al_yGa_{1-y}As$-GaAs-$In_xGa_{1-x}As$ quantum well heterostructure laser," *Appl. Phys. Lett.*, vol. 63, no. 12, pp. 1660–1662, 1993.

[48] E. I. Chen, N. Holonyak, and S. A. Maranowski, "$Al_xGa_{1-x}As$-GaAs metal-oxide semiconductor field effect transistors formed by lateral water vapor oxidation of AlAs," *Appl. Phys. Lett.*, vol. 66, no. 20, pp. 2688–2690, 1995.

[49] M. J. Ries, T. A. Richard, S. A. Maranowski, N. Holonyak, and E. I. Chen, "Photopumped room-temperature edge- and vertical-cavity operation of AlGaAs-GaAs-InGaAs quantum-well heterostructure lasers utilizing native oxide mirrors," *Appl. Phys. Lett.*, vol. 65, no. 6, pp. 740–742, 1994.

[50] M. H. MacDougal, H. Zhao, P. D. Dapkus, M. Ziari, and W. H. Steier, "Wide bandwidth distributed Bragg reflectors using oxide/GaAs multilayers," *Electron. Lett.*, vol. 30, pp. 1147–1149, 1994.

[51] K. Tai, K. W. Wang, S. N. G. Chu, and A. Y. Cho, "Use of implant isolation for fabrication of vertical cavity surface-emitting laser diodes," *Electron. Lett.*, vol. 25, no. 24, pp. 1644–1645, Nov. 1989.

[52] K. Tai, L. Yang, Y. H. Wang, J. D. Wynn, and A. Y. Cho, "Drastic reduction of series resistance in doped semiconductor distributed Bragg reflectors for surface-emitting lasers," *Appl. Phys. Lett.*, vol. 56, no. 25, pp. 2496–2498, 1990.

[53] D. L. Huffaker, D. G. Deppe, K. Kumar, and T. J. Rogers, "Native-oxide defined ring contact for low threshold vertical-cavity lasers," *Appl. Phys. Lett.*, vol. 65, no. 1, pp. 97–99, 1994.

[54] J. M. Dallesasse and D. G. Deppe, "III–V Oxidation: Discoveries and applications in vertical-cavity surface-emitting lasers," *Proc. IEEE*, vol. 101, no. 10, pp. 2234–2242, Oct. 2013.

[55] K. D. Choquette, R. P. Schneider, K. L. Lear, and K. M. Geib, "Low threshold voltage vertical-cavity lasers fabricated by selective oxidation," *Electron. Lett.*, vol. 30, no. 24, pp. 2043–2044, Nov. 1994.

[56] S. B. Healy *et al.*, "Active region design for high-speed 850 nm VCSELs," *IEEE J. Quantum Electron.*, vol. 46, no. 4, pp. 506–512, Apr. 2010.

[57] Y. Ou, J. S. Gustavsson, P. Westbergh, A. Haglund, A. Larsson, and A. Joel, "Impedance characteristics and parasitic speed limitations of high-speed 850-nm VCSELs," *IEEE Photon. Technol. Lett.*, vol. 21, no. 24, pp. 1840–1842, Dec. 15, 2009.

[58] P. Westbergh, J. S. Gustavsson, Â. Haglund, M. Skold, A. Joel, and A. Larsson, "High-speed, low-current-density 850 nm VCSELs," *IEEE J. Sel. Top. Quantum Electron.*, vol. 15, no. 3, pp. 694–703, Mar./Jun. 2009.

[59] Y. C. Chang, C. S. Wang, and L. A. Coldren, "High-efficienc, high-speed VCSELs with 35 Gbit=s error-free operation," *Electron. Lett.*, vol. 43, no. 19, pp. 1022–1023, Sep. 2007.

[60] S. A. Blokhin *et al.*, "Oxide-confined 850 nm VCSELs operating at bit rates up to 40 Gbit/s," *Electron. Lett.*, vol. 45, no. 10, pp. 501–503, May 2009.

[61] D. M. Kuchta *et al.*, "A 55 Gb/s directly modulated 850 nm VCSEL-based optical link," in *Proc. IEEE Photon. Conf.*, Burlingame, CA, USA, Sep. 2012, pp. 1–2, paper PD 1.5.

[62] D. M. Kuchta *et al.*, "A 50 Gb/s NRZ modulated 850 nm VCSEL transmitter operating error free to 90 °C," *J. Lightw. Technol.*, vol. 33, no. 4, pp. 802–810, Feb. 15, 2015.

[63] X. Yang, M. Li, G. Zhao, Y. Zhang, S. Freisem, and D. Deppe, "Small-sized lithographic single-mode VCSELs with high-power conversion efficiency," *Proc. SPIE, Vertical-Cavity Surf.-Emitting Lasers XIX*, vol. 9381, p. 93810R, Mar. 2015.

[64] J. Leshin *et al.*, "Lithographic VCSEL array multimode and single mode sources for sensing and 3D imaging," *Proc. SPIE, Image Sens. Technol., Mater., Devices, Syst., Appl. III*, vol. 9854, p. 98540Y, May 2016.

[65] M. Li, X. Yang, N. Cox, J. Beadsworth, and D. Deppe, "Record low differential resistance using lithographic VCSELs," in *Proc. Conf. Lasers Electro-Opt.*, San Jose, CA, USA, Jun. 2016, pp. 1–2.

[66] G. Walter, N. Holonyak, M. Feng, and R. Chan, "Laser operation of a heterojunction bipolar light-emitting transistor," *Appl. Phys. Lett.*, vol. 85, no. 20, pp. 4768–4770, 2004.

[67] M. Feng, N. Holonyak, G. Walter, and R. Chan, "Room temperature continuous wave operation of a heterojunction bipolar transistor laser," *Appl. Phys. Lett.*, vol. 87, no. 13, p. 131103, 2005.

[68] M. Feng, H. W. Then, N. Holonyak, G. Walter, and A. James, "Resonance-free frequency response of a semiconductor laser," *Appl. Phys. Lett.*, vol. 95, no. 3, p. 033509, 2009.

[69] G. Walter, C. H. Wu, H. W. Then, M. Feng, and N. Holonyak, Jr., "4.3 GHz optical bandwidth light emitting transistor," *Appl. Phys. Lett.*, vol. 94, no. 24, p. 241101, 2009.

[70] G. Walter, C. H. Wu, H. W. Then, M. Feng, and N. Holonyak, "Tilted-charge high speed (7 GHz) light emitting diode," *Appl. Phys. Lett.*, vol. 94, no. 23, p. 231125, 2009.

[71] M. Feng, C.-H. Wu, C.-H. Wu, and N. Holonyak, "Resonance-free optical response of a vertical cavity transistor laser," *Appl. Phys. Lett.*, vol. 111, no. 12, p. 121106, 2017.

[72] E. M. Purcell, "Spontaneous emission probabilities at radio frequencies," *Phys. Rev.*, vol. 69, no. 11, p. 681, 1946.

[73] L. A. Graham, D. L. Huffaker, Q. Deng, and D. G. Deppe, "Controlled spontaneous lifetime in microcavity confined InGaAlAs/GaAs quantum dots," *Appl. Phys. Lett.*, vol. 72, no. 14, p. 1670–1672, 1998.

[74] L. A. Graham, D. L. Huffaker, and D. G. Deppe, "Spontaneous lifetime control in a native-oxide-apertured microcavity," *Appl. Phys. Lett.*, vol. 74, no. 17, p. 2408–2410, 1999.

[75] J.-M. Gerard and B. Gayral, "Strong Purcell effect for InAs quantum boxes in three-dimensional solid-state microcavities," *J. Lightw. Technol.*, vol. 17, no. 11, pp. 2089–2095, Nov. 1999.

[76] T. Baba and D. Sano, "Low-threshold lasing and Purcell effect in microdisk lasers at room temperature," *IEEE J. Sel. Topics Quantum Electron.*, vol. 9, no. 5, pp. 1340–1346, Sep. 2003.

[77] D. E. McCumber, "Intensity fluctuations in the output of cw laser oscillators. I," *Phys. Rev.*, vol. 141, no. 1, p. 306, Jan. 1966.

[78] M. Lax, "Quantum noise VII: The rate equations and amplitude noise in lasers," *IEEE J. Quantum Electron.*, vol. 3, no. 2, pp. 37–46, Feb. 1967.

[79] G. P. Agrawal, "Mode-partition noise and intensity correlation in a two-mode semiconductor laser," *Phys. Rev. A, Gen. Phys.*, vol. 37, no. 7, p. 2488, Apr. 1988.

[80] C. B. Su, J. Schlafer, and R. B. Lauer, "Explanation of low-frequency relative intensity noise in semiconductor lasers," *Appl. Phys. Lett.*, vol. 57, no. 9, pp. 849–851, Jun. 1990.

[81] H. Statz and G. deMars, *Quantum Electronics*. New York, NY, USA: Columbia Univ. Press, 1960, p. 650.

[82] D. D. Sell, H. C. Casey, and K. W. Wecht, "Concentration dependence of the refractive index for *n*- and *p*-type GaAs between 1.2 and 1.8 eV," *J. Appl. Phys.*, vol. 45, no. 6, pp. 2650–2657, 1974.

[83] J. Manning, R. Olshansky, and S. Chin, "The carrier-induced index change in AlGaAs and 1.3 μm InGaAsP diode lasers," *IEEE J. Quantum Electron.*, vol. QE-19, no. 10, pp. 1525–1530, Oct. 1983.

[84] M. Razeghi, *The MOCVD Challenge: A Survey of Gainasp-Inp and Gainasp-Gaas for Photonic and Electronic Device Applications*. Boca Raton, FL, USA: CRC Press, 2011.

[85] C.-T. Tsai *et al.*, "Multi-mode VCSEL chip with high-indium-density InGaAs/AlGaAs quantum-well pairs for QAM-OFDM in multi-mode fiber," *IEEE J. Quantum Electron.*, vol. 53, no. 4, Aug. 2017, Art. no. 2400608.

[86] H.-Y. Kao *et al.*, "Comparison of single-/few-/multi-mode 850 nm VCSELs for optical OFDM transmission," *Opt. Exp.*, vol. 25, no. 14, pp. 16347–16363, 2017.

[87] H.-Y. Kao *et al.*, "Few-mode VCSEL chip for 100-Gb/s transmission over 100 m multimode fiber," *Photon. Res.*, vol. 5, no. 5, pp. 507–515, 2017.

Milton Feng (F'92–LF'17) received the B.S. degree in electrical engineering from Columbia University, New York, in 1973, and the M.S. and Ph.D. degrees in electrical engineering from the University of Illinois Urbana–Champaign, in 1976 and 1979, respectively. From 1979 to 1983, he was the Head of the GaAs material and device Group, Torrance Research Center, Hughes Aircraft Company, where he was an In charge of ion implantation, $AsCl_3$ VPE, MOCVD, and MBE Technology. In 1983, he developed a direct ion-implanted low-noise and power MESFET and MMICs for X-band phase array radar application. He demonstrated the first 60-GHz GaAs amplifiers in 1983. From 1984 to 1986, he was with Ford Microelectronics Inc., Colorado Springs, CO, USA, where he managed the advanced digital integrated circuit development program in 1 K SRAM and 500 gate arrays.

Since 1991, he has been a Professor of electrical and computer engineering and a Research Professor with the Microelectronics Laboratory, University of Illinois at Urbana–Champaign. He is currently a Holonyak Endowed Chair Professor of electrical and computer engineering. He invented the pseudomorphic HBT (PHBT), pushed the transistor speed boundary toward THz, and demonstrated InP PHBTs with the world's fastest speed performance (> 800 GHz). He along with Prof. N. Holonyak, Jr., demonstrated the first laser operation of a quantum-well-based light emitting transistor and a transistor laser. The transistor laser opens up a rich domain of integrated circuitry and high-speed signal processing that involves both electrical and optical signals. Since 2010, he has been the Leader in both high-speed oxide-confined VCSEL for optical interconnect and Type II InP DHBT power amplifier and ICs for 5G Wireless Communications.

He has authored or co-authored over 250 papers, 220 conference talks, and been granted 39 U.S. patents in semiconductor microelectronics and photonics. He is an OSA Fellow, and serves on many executive and strategy committees both in industry and at conferences. In 1989, he received the Ford Aerospace Corporate Technology Outstanding Principal Investigator Award for his contribution of advancing ion implantation GaAs and InGaAs MESFETs into manufacturable millimeter-wave ICs. He was a recipient of the IEEE field award—David Sarnoff Award—in 1997, the Pan Wen Yuan Outstanding Research Award in microelectronics in 2000, and the Distinguished ECE Alumni Award, University of Illinois at Urbana-Champaign, in 2017. In 2013, he received the Optical Society R. W. Wood Prize for the co-invention and realization of the transistor laser. In 2005, he was chosen as the first Holonyak Chair Professor of electrical and computer engineering. In 2006, his transistor laser research paper was selected as one of the top five papers in the 43-year history of *Applied Physics Letters*, and also was selected as one of the 100 top most important discoveries in 2005 by *Discover* magazine.

Chao-Hsin (Wayne) Wu (S'03–M'04) received the B.S. and M.S. degrees in electrical engineering from National Taiwan University, Taipei, Taiwan, in 2002 and 2004, respectively, and the Ph.D. degree in electrical and computer engineering from the University of Illinois at Urbana–Champaign, USA, in 2010. He is currently an Associate Professor with the Department of Electrical Engineering, Graduate Institute of Photonics and Optoelectronics, and Graduate Institute of Electronics Engineering, National Taiwan University, Taipei, Taiwan.

Before joining Prof. M. Feng and Prof. N. Holonyak Jr., at UIUC, he used to work as a full-time Teaching Assistant In charge of the Automatic Control Laboratory, Department of Electrical Engineering, National Taiwan University, from 2005 to 2006. He was a Post-Doctoral Research Fellow before he joined as a Faculty Member with National Taiwan University in 2011. In Illinois, he pioneered the development of novel III–V high-speed microelectronics and optoelectronics devices, including InGaN/GaN heterojunction bipolar transistors, InGaP/GaAs power amplifiers, and microcavity lasers. His research mainly focuses on the three-terminal light-emitting transistors and transistor lasers. He has demonstrated the world-record optical spontaneous modulation bandwidth of 7 GHz (corresponding to a recombination lifetime of 23 ps), which is a breakthrough in semiconductor device technology history for the past 47 years. He has authored or co-authored over 40 journal papers and 60 conference papers. His current research at National Taiwan University includes high-speed VCSELs for optical interconnects, GaN-on-Si power and rf electronics, 2-D material field-effect transistors, Si photonics, transistor lasers for optical logic gates, and GaN LED for visible light communications.

Dr. Wu is also a member of SPIE and OSA. He was a recipient of the Nick and Katherine Holonyak, Jr. Award from UIUC in 2010. He was an Irving T. Ho Outstanding Young Scholar and received the Academic Contribution Award from EECS College, National Taiwan University, in 2017.

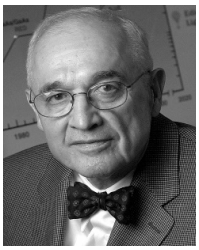

Nick Holonyak, Jr. (LF'94) was born in Zeigler, IL, USA, in 1928. He received the B.S., M.S., and Ph.D. degrees in EE from the University of Illinois at Urbana–Champaign, in 1950, 1951, and 1954, respectively. He was John Bardeen's first student and held a TI Fellowship. He was with the Bell Telephone Laboratories from 1954 to 1955.After military service, he was with GE, Syracuse, from 1957 to 1963. He was with the University of Illinois at Urbana–Champaign in 1963. He is currently a John Bardeen Chair Professor of electrical and computer engineering and physics, and an ECE Professor with the Center of Advanced Study.

He is an early contributor to diffused-impurity oxide-masked silicon device technology (transistors, p-n-p-n switches, and thyristors), the technology basic to the integrated circuit from 1954 to 1960. He was the inventor of the shorted emitter used in thyristors and symmetrical switches, including the basic element in the wall light dimmer in 1958. He was the first to make silicon tunnel diodes and observe phonon-assisted tunneling, the first observation of inelastic tunneling and the beginning of tunneling spectroscopy in 1959. He invented closed-tube vapor phase epitaxy of III–V semiconductors, the forerunner of present-day open-tube III–V VPE crystal growth in 1960. Besides early work on III–V heterojunctions, he was the first to grow $GaAs_{1-x}P_x$ (an alloy) in 1960 and to construct visible-spectrum lasers and light emitting diodes in 1962, thus proving that III-V alloys are smooth and viable, in general, for use in optoelectronic devices. He is the inventor of the first practical LED, the red $GaAs_{1-x}P_x$ LED, which (based on its diode laser extension) led to the concept of an ultimate lamp and marks also the beginning in the use of III-V alloys in semiconductor devices, including in heterojunctions and quantum well heterostructures. Besides demonstrating the visible-spectrum laser operation of the alloys GaAsP in 1962, InGaP (1970), AlGaAsP (1970), and InGaPAs (1972), he and his student Rezek made (via LPE, 1977) the first quantum well (QW) diode lasers. Later, with Dupuis (and MOCVD AlGaAs-GaAs), he demonstrated the initial continuous 300 K operation of a QW laser, and introduced the name quantum well laser in 1978. He and his students introduced impurity-induced disordering and intermixing ($\sim$ 600° C) of QW heterostructure and superlattice layers, and with it the selective shift from QW lower gap to bulk-crystal higher gap (used to define waveguide and laser geometries) in 1980. In 1990, he and his students introduced the Al-based III–V native oxide into optoelectronics, including its use as a buried oxide aperture to define the current and cavity in lasers (now used in VCSELs). He (with Dupuis) introduced coupled quantum-dot/quantum-well lasers, and with M. Feng introduced light-emitting heterojunction bipolar transistors modified with quantum well base regions and reinvented the transistor as a transistor laser in 2004. His work has led to over 574 papers and 55 patents.

Dr. Holonyak is a member of the National Academy of Engineering in 1973, National Academy of Sciences in 1984, a fellow of the American Academy of Arts and Sciences in 1984, a Foreign Member of the Russian Academy of Sciences in 1999, a fellow of the American Physical Society, a fellow of the Optical Society of America, and a fellow of the American Association for the Advancement of Science, the Electrochemical Society, and the Mathematical Association of America. He was a recipient of a number of awards, including: the Cordiner Award from GE in 1962; the Morris N. Liebmann Award from IEEE in 1973; the John Scott Medal from City of Philadelphia in 1975; the Gallium Arsenide Symposium Award with Welker Medal in 1976; the Jack A. Morton Award from IEEE in 1981; the Solid State Science and Technology Award from the Electrochemical Society in 1983; the Monie A. Ferst Award from Sigma Xi in 1988; the Edison Medal from IEEE in 1989; the National Medal of Science, U.S., in 1990; the Charles H. Townes Award from OSA in 1992; the Honorary Member of the Ioffe Physical-Technical Institute, St. Petersburg, in 1992; the Honorary Doctor of Science, Northwestern University in 1992; the NAS Award for the Industrial Application of Science in 1993; ASEE Centennial Medal in 1993; the American Electronics Association 50th Anniversary Award in 1993; the Vladimir Karapetoff Eminent Members' Award of Eta Kappa Nu in 1994; Honorary Doctor of Engineering, Notre Dame, 1994; the TMS John Bardeen Award from The Minerals, Metals, and Materials Society in 1995; Japan Prize in 1995; Eminent Member of Eta Kappa Nu in 1998; Distinguished Alumnus of Tau Beta Pi in 1999; the IEEE Third Millennium Award in 2000; Frederic Ives Medal of the Optical Society of America in 2001; Global Energy International Prize, Russia, in 2003; the IEEE Medal of Honor in 2003; National Medal of Technology (2002 Medal, awarded in 2003); the Washington Award from the Western Society of Engineers, in 2004; Lemelson–MIT Prize in 2004; the MRS Von Hippel Award in 2004; the Izaak Walton League of America Illinois Division Energy Conservation Award in 2004; Laureate of the Lincoln Academy of Illinois in 2005; Member of the Consumer Electronics Association Hall of Fame in 2006; National Inventors Hall of Fame in 2008; The Engineering at Illinois Hall of Fame in 2010; and Engineering and Science Hall of Fame in 2011. In 2015, he was also a recipient of the NAE Charles Stark Draper Prize and elected to prestigious OSA Honorary member.